DEVELOPMENT OF A CROSS-PLATFORM ALGORITHM FOR APPLICATION OF DIGITAL HOLOGRAPHY IN 3D PARTICLE DETECTION

A Thesis

Submitted to the Faculty

of

Purdue University

by

Yijie Wang

In Partial Fulfillment of the

Requirements for the Degree

of

Master of Science in Mechanical Engineering

August 2019

Purdue University

West Lafayette, Indiana

THE PURDUE UNIVERSITY GRADUATE SCHOOL
STATEMENT OF THESIS APPROVAL

Dr. Jun Chen, Chair

School of Mechanical Engineering

Dr. Paul E. Sojka

School of Mechanical Engineering

Dr. Song Zhang

School of Mechanical Engineering

Approved by:

Dr. Jay P. Gore

Head of the Graduate Program

For my family.

ACKNOWLEDGMENTS

It is one of my most precious experiences to study at Purdue University as a graduate student. The wonderful scholars and helpful faculties make my life in West Lafayette memorable.

First of all, I would like to thank Professor Jun Chen, my chair advisor. He offered me the opportunity to continue my research and pursue a degree at Purdue University. With his rich experiences and reliable support, I am able to complete my degree. His guidance teaches me how to do research independently and how to be professional.

I also give my grateful thanks to the rest of my committee members, Professor Paul E. Sojka and Professor Song Zhang, for their helpful advice and their time to read my thesis.

Furthermore, I would like to thank Longchao Yao, a visiting scholar from Zhejiang University. His generous guidance on coding is appreciated.

I must thank my lab-mates as well as my roommates, Weixiao Shang and Puyuan Wu for their help on experiment setup and the relief they provided when I am stressed. The colleagues in Dr. Chen's group, including Ang Li, Dazhuang He, and Zechao Lu, are appreciated for their enlightened discussion with me on my experiments.

TABLE OF CONTENTS

Page

LIST OF TABLES

LIST OF FIGURES

Figure Page

ABBREVIATIONS

2D	two-dimensional
3D	three-dimensional
CC	correlation coeffcient
CCD	charge-coupled device
CDP	cumulative density function
CMOS	complementary metal-oxide-semiconductor
CPU	central processing unit
DC	direct current
DH	digital holography
DHM	digital holographic microscopy
DIH	digital in-line holography
EDOF	extended depth of focus
FFT	fast Fourier transform
GPU	graphics processing unit
LAP	laplacian
MEI	minimum edge intensity
MI	minimum intensity
MPI	message passing interface
OOP	object oriented programming
PDA	phase Doppler anemometry
PDF	probability density function
PIV	particle image velocimetry
PMP	pearl mica powder
RAM	random-access memory
SP	solder powder

TON	time optimization number
VAR	variance
WP	wollationite powder

NOMENCLATURE

A	image amplitude
A_p	area of the particle
C	circularity
D_{32}	Sauter mean diameter
D_{eq}	equivalent diameter
D_t	true diameter
e	error
E	complex amplitude
f_x	spatial frequency in x direction
f_y	spatial frequency in y direction
g	Rayleigh-Sommerfeld diffraction kernel
h	hologram
I	intensity
$\bar{I}_W$	mean intensity in a window
$\bar{I}_P$	mean intensity inside a particle
j	imaginary unit
J_0	zero-order Bessel's function
k	wave number
K	magnification
m	pixel-wise horizontal dimension in hologram
M	pixel number in horizontal direction
n	pixel-wise vertical dimension in hologram
N	pixel number in vertical direction
N_{Edge}	number of the edge pixels of a particle
N_{tot}	total number of particles in a particle field

O	object signal
p	pixel-wise horizontal dimension in image plane
P_p	perimeter of the particle
q	pixel-wise vertical dimension in image plane
R	reference signal
R_d	detection rate
R_{fs}	false separation rate
R_m	missing rate
R_t	Ray transfer matrix
S	edge sharpness
SD	shadow density
S_x	horizontal Sobel kernel
S_y	vertical Sobel kernel
t	global threshold
$t_{0,i}$	local threshold for the ith window
t'	optimized threshold
T	Tenegrad map
x	horizontal dimension in image plane
x_t	true horizontal position
y	vertical dimension in image plane
y_t	true vertical position
Δx	horizontal pixel size in image plane
Δy	vertical pixel size in image plane
z	dimension in the light propagation direction
z_0	actual position of the particle in z direction
z_{eq}	equivalent distance
z_m	depth corresponding to the minimum intensity
Z	inverse of the Fresnel number
ξ	horizontal dimension in hologram

η	vertical dimension in hologram
$\Delta\xi$	horizontal pixel size in hologram
$\Delta\eta$	vertical pixel size in hologram
θ	angle between object wave and reference wave
λ	wavelength
σ^2	size of the wavelet
ρ	normalized radial coordinate
γ	aspect ratio

ABSTRACT

Wang, Yijie M.S.M.E, Purdue University, August 2019. Development of a Cross-platform Algorithm for Application of Digital Holography in 3D Particle Detection. Major Professor: Jun Chen, School of Mechanical Engineering.

Digital holography (DH) has a variety of applications on measuring the 3D position of different kinds of particles, including the droplets created in drop breakups, seeding particles for flow velocity measurements, characterizations of the behavior of the microorganisms, etc. A particle detection method is required to extract the 3D information encoded in the interference patterns of the holograms, which is desired to be accurate and fast. As the accuracy of the particle detection method improves, the time efficiency of the method decreases. In this study, an optimization process is developed based on an existing method to shorten the processing time. The optimization process includes reducing the complexity of the method and introducing the parallel processing algorithm that can be implemented on cluster machines. The existing particle detection method is separated into several steps and analyzed. The most time consuming step, refining the threshold to separate overlapping particles, is the focus of complexity reduction optimization. A Python code is developed, based on object oriented programming, to implement the optimization. Message Passing Interface (MPI) is applied for parallel processing with a 24-core remote workstation. The optimized Python code is compared with the existing Matlab code in both time consumption and accuracy aspects with synthetic holograms. It is found that the optimization process is able to reduce the time consumption by about four times with an acceptable sacrifice in accuracy. Finally, a DIH system with the optimized method, is applied to characterize different kinds of solid particles. One is noted that the previous studies focus on measuring artificial particles or droplets which are both spherical particles, while most natural solid particles usually have irregular shapes. Equivalent diameter, circularity and aspect ratio are introduced to quantify the dimension and morphology of the irregular shapes. The statistics

of the parameters are generated to characterize different kinds of the particles. The accuracy of the characterization of the particles are verified with the observation of the microscopic images of the particles, which can further prove the improvement of the optimized method for particle detection.

1. INTRODUCTION

The quantitative characteristics of small particles, whose diameters range from tens to hundreds of micrometers need to be measured in many applications. These applications include the study of multiphase flows, such as droplets from liquid breakup and bubbles from cavitation, where the morphology and dynamics of these droplets and bubbles are often of interest. The study of the droplets breakup process is essential to the research of atomization and sprays (Ashgriz, 2011) and the study of the separation process in cyclone separators (Wang et al., 2017). The control of the formation and the collapse of the bubbles are important to the performance of micro-rotors (Yang et al., 2017) and are often related to acoustic studies (Leighton, 2012). Moreover, the dimension and morphology of solid particles have a significant effect on the industrial applications, such as the performance of the coating process (Rawle, 2002) and the assessment of industrial air pollution (Al-Rajhi et al., 1996). In chemical engineering, tiny particles are investigated in terms of their morphology and concentration. The energy efficiency of coal combustion is determined by the dimension distribution and concentration of the pulverized coal particles (Wu et al., 2017). To visualize flows, tracking particles are often seeded into the flow. The displacement of these particles measured by Particle Image Velocimetry (PIV) are determined to represent the movement of the flow (Raffel et al., 2018). There are various other studies where the morphology, size, 3D position and velocity of the particles are the main characteristics concerned in these studies.

Point-wise techniques are commonly used for quantifying the characteristics of particles. For example, the Phase Doppler anemometry (PDA) can measure the dimension and 3D velocity of the particles passing the intersection point of multiple laser beams. The velocity of the particles are measured from the Doppler shift of the laser beam. 2D images techniques are applied to expand the measurement from a point to a plane, such as shadowgraphy. By introducing a bright background, the shadowgraphs of the particles are taken, where the sizes, shapes, and positions of the particles on the focal plane of the camera lens can be measured.

However, the particles out of the focal plane are also taken in the shadowgraph, which are out-of-focus and cannot be measured. A laser sheet is introduced to only illuminate the particles on the focal plane. In experimental fluid dynamics, PIV is developed to measure the 2D velocity field of the flow by introducing tracking particles. PIV uses a laser sheet to illuminate the tracking particles on the focal plane of the camera lens. The images of illuminated particles are captured in a small time step. By computing the cross-correlation between images, the 2D velocity field can be determined (Raffel et al., 2018). By contrast, many physical processes are three dimensional so a method to measure the spatial quantitative characteristics of a 3D particle field in is preferred.

On the other hand, holography provides a spatially resolved 3D measurement of particle field. By recording the holograms at consecutive time steps, the 3D velocity of the particles can be measured as well. By adopting the digital holography processing, the experiment setup is significantly simplified compared to the analog holography. Thus, digital holography (DH) is becoming more commonly used to measure various solid, liquid and gas particles with a simple setup.

In this thesis, the steps of the digital holography (DH) is reviewed and developed. The time efficiency of the current particle detection algorithm is analyzed and optimized by reducing the complexity of the algorithm, introducing parallel processing and cross-platform algorithm. A DH system is applied to quantify the dimension and morphology of natural solid particles.

This thesis is organized as following. In Chapter 2, the principles and applications of digital holography are introduced. In Chapter 3, the principles of the existing particle detection methods are reviewed. In Chapter 4, the objectives and motivations of the paper is presented. In Chapter 5, the detailed description of the optimization method is presented and the processing time and accuracy tests methods are included. Also, the test results are discussed. In Chapter 6, the application of DH to measure the natural solid particles is presented. In Chapter 7, the optimization of the setup of the lensed DIH system is discussed. Finally, the conclusions are made in Chapter 8.

2. DIGITAL HOLOGRAPHY

2.1 Principle to Holography

The concept of holography was first introduced by Gabor (Gabor, 1948) in 1948. In a standard holography system, there are two steps in holography: recording and reconstruction. The 3D position information is recorded as interference patterns on a single 2D image (hologram) in the recording step. In the reconstruction step, the 3D position is extracted from the hologram at different depth positions. Thus, compared to traditional photography, holography allows people to acquire the 3D image of an object by recording a 2D hologram.

In the recording step, a coherent light source illuminates the object. The light reflected or diffracted by the object serves as the object light. The reference light comes from another beam of the same light source. The intensity patterns of the interference formed by the object light and the reference light, which is recorded, is the hologram plane, as illustrated in Fig. 2.1 (a). (Schnars and Jueptner, 2005). The mathematical expression of the recorded hologram on the hologram plane is

$$\begin{aligned} h(\xi,\eta) =& |O(\xi,\eta) + R(\xi,\eta)|^2 \\ =& |O(\xi,\eta)|^2 + |R(\xi,\eta)|^2 + O(\xi,\eta)R^*(\xi,\eta) + O^*(\xi,\eta)R(\xi,\eta), \end{aligned} \tag{2.1}$$

where O and R denote to the complex amplitude of the Object Wave and Reference Wave. O^* and R^* are their complex conjugates, respectively.

In the reconstruction process, the target is to retrieve the object wave, O, or the conjugate, O^*. To achieve the retrieving process, the complex conjugate of the reference wave, R^* , illuminates the hologram. The emerged wave propagates to an image plane and forms a focused image of the object, as Fig. 2.1 (b) illustrated. Mathematically, the illuminating part of the reconstruction process can be written as the multiplication of the complex amplitude of hologram from Equation 2.1 and the conjugate of the reference wave R^*:

$$R^*(\xi,\eta)h(\xi,\eta) = (|O|^2 + |R|^2)R^* + OR^{*2} + O^*|R|^2. \tag{2.2}$$

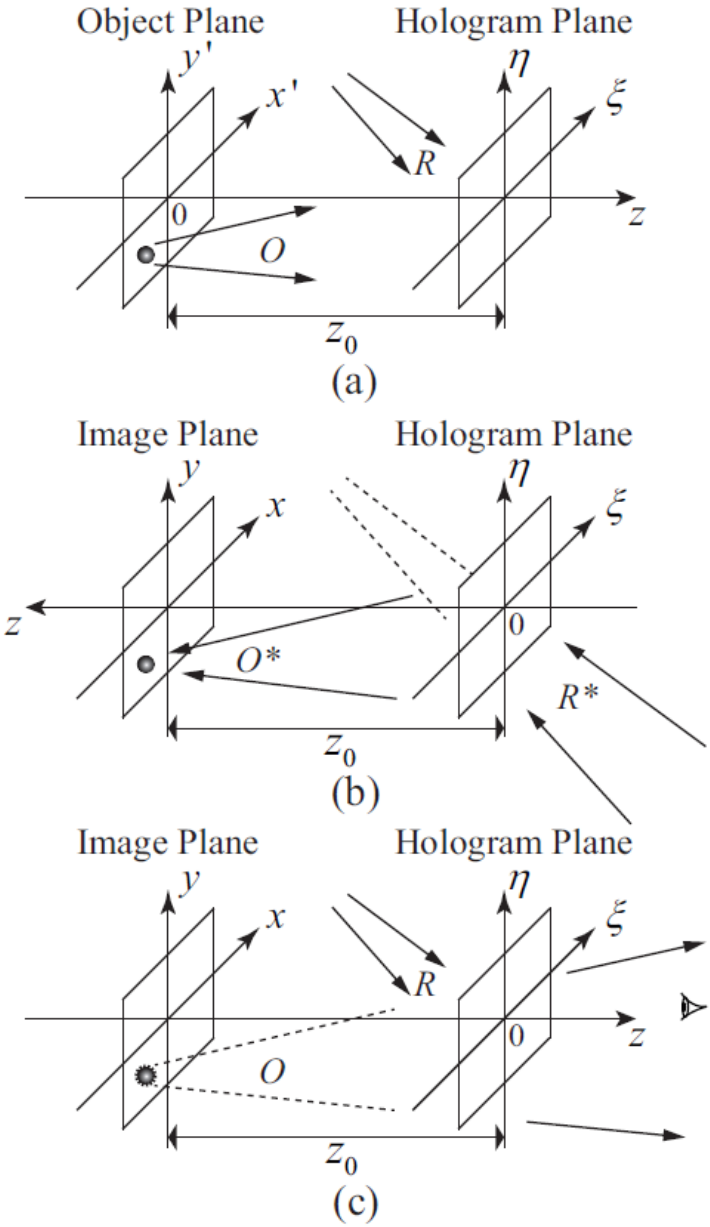

Figure 2.1. The recording and reconstruction process of the hologram. (Schnars and Jueptner, 2005) (a) recording process. (b) The reconstruction process by the complex conjugate of the reference light. (c) The reconstruction process by the original reference light.The z-direction is the light propagation direction in the coordinate system.

The result of the multiplication in Equation 2.2 is the complex amplitude of the emerged wave. Equation 2.2 gives the reconstructed complex amplitude in the hologram plane ($z = 0$) on the right-hand side. $|O|^2 + |R|^2)R^*$ is the DC term, which corresponds to the background after the reconstruction process. OR^{*2} is the twin image term that gives an out-of-focus virtual image. This term is usually undesirable in the application of the holography. The last term $O^*|R|^2$ is the complex amplitude of real image. Because the reference light is usually a uniform distribution on the hologram plane, the term $|R|^2$ is a constant which is excluded in the following equations. So the term O^* carries the information of the object wave and propagates to the image plane.

Then the emerged light propagates to an image plane which has a distance z from the hologram plane. The complex amplitude at each point (x, y) in the image plane can be expressed by the integration of light propagated from every point in the hologram plane (Goodman, 2005):

$$E(x, y, z) = \iint_{-\infty}^{+\infty} h(\xi, \eta) R^*(\xi, \eta) \frac{1}{j\lambda} \frac{\exp[jk\sqrt{(x-\xi)^2 + (y-\eta)^2 + z^2}]}{\sqrt{(x-\xi)^2 + (y-\eta)^2 + z^2}} d\xi d\eta, \tag{2.3}$$

where $E(x, y, z)$ is the complex amplitude in the image plane. λ denotes the wavelength of light and k denotes the wave number. The fracture part in Equation 2.3 is the mathematical expression of the propagation from Rayleigh-Sommerfeld diffraction equation. It can be rewritten in the convolution expression by

$$E(x, y, z) = [h(\xi, \eta) R^*(\xi, \eta)] \otimes g(\xi, \eta, z), \tag{2.4}$$

where $\otimes$ refers to convolution operation and $g(\xi, \eta, z)$ is the Rayleigh-Sommerfeld diffraction kernel,

$$g(\xi, \eta, z) = \frac{1}{j\lambda} \frac{e^{jk\sqrt{\xi^2+\eta^2+z^2}}}{\sqrt{\xi^2 + \eta^2 + z^2}}. \tag{2.5}$$

Similar to Equation 2.4, the recording processing can be mathematically expressed as well. Assume a object at the object plane whose distance to the hologram plane is z_0 and the object wave is $O'(x', y')$. The object wave propagates to the hologram plane to get the complex amplitude in the hologram plane $O(\xi, \eta)$, which can be expressed by

$$O(\xi, \eta) = O'(x', y') \otimes g(x', y', z_0). \tag{2.6}$$

To calculate convolution operation in Equation 2.4 and 2.6, the Fourier transform is applied to these equations. The convolution operation will get to multiplication in the frequency domain. It is noticed that the Fourier transform of the diffraction kernel has an analytical expression (Goodman, 2005),

$$\mathcal{F}\{g(\xi,\eta,z)\} = G(f_x,f_y,z) = \exp\left(jkz\sqrt{1-\lambda^2 f_x^2-\lambda^2 f_y^2}\right) \tag{2.7}$$

where $\mathcal{F}\{\}$ is the Fourier transform operation. f_x and f_y denotes the planar coordinate system in frequency domain. The Fourier transform of the complex amplitude is

$$\mathcal{F}\{O\} = \mathcal{F}[O'](f_x,f_y)G(f_x,f_y,z_0), \tag{2.8}$$

As discussed above, the conjugate of the complex amplitude in the hologram plane, O^*, is what needed for the reconstruction. With the properties of the Fourier transform, the Fourier transform of the complex conjugate in the hologram plane can be expressed by

$$\mathcal{F}\{O^*\} = (\mathcal{F}\{O\}(-f_x,-f_y))^*. \tag{2.9}$$

Incorporating Equation 2.8, the Fourier transform can be rewritten (Goodman, 2005)

$$\mathcal{F}\{O^*\} = \mathcal{F}^*\{O'\}(-f_x,-f_y)G(f_x,f_y,z_0), \tag{2.10}$$

where $\mathcal{F}^*\{\}$ denotes to the complex conjugate of the Fourier transform.

Then, in reconstruction process, by combining Equation 2.4 and Equation 2.10, the complex amplitude in the image plane can be written as

$$\begin{aligned} E(x,y,z) &= O^*(\xi,\eta)\otimes g(\xi,\eta,z) \\ &= \mathcal{F}^{-1}\{\mathcal{F}^*\{O'\}(-f_x,-f_y)G(f_x,f_y,(z-z_0))\} \\ &= \mathcal{F}^{-1}\left\{\mathcal{F}^*\{O'\}(-f_x,-f_y)\exp\left[jk(z-z_0)\sqrt{1-\lambda^2 f_x^2-\lambda^2 f_y^2}\right]\right\}, \end{aligned} \tag{2.11}$$

where $\mathcal{F}^{-1}\{\}$ refers to the inverse Fourier transform operation.It is noticed that only when $z=z_0$, $G(f_x,f_y,(z-z_0))=1$. And Equation 2.11 turns to

$$E = \mathcal{F}^{-1}\{\mathcal{F}^*\{O'\}(-f_x,-f_y)\} = O'^*, \tag{2.12}$$

which shows that the complex amplitude in the image plane E is the same as the conjugate of the object wave O'^*. The real image which gives $|O'|^2 = |O'^*|^2$ will lead to a focused image on the image plane.

Alternatively, as Fig. 2.1 (c) shown, using the reference wave (R) directly for reconstruction is similar. The virtual image will be focused at $-z_0$ which means the image is on the opposite side.

2.2 In-line Setup versus Off-axis Setup

There are two categories of setups of holography, in-line setup and off-axis setup. In the in-line setup, the object wave and reference wave propagate in the same direction. In an off-axis setup, there is an angle between the object wave and reference wave. The recording processes of these two setups are shown in Fig. 2.2 (a) and (b), respectively. A plane wave serves as both the object wave and the reference wave in in-line setup. The wave diffracted by the object is the object wave. The rest part of the wave is the reference wave. In off-axis setup, the object wave also comes from the diffracted light by the object, but a tilted plane wave serves as the reference wave.

In the reconstruction process, the reference wave illuminates the hologram as shown in Fig. 2.2 (c) and (d). The process can be mathematically expressed as Equation 2.2. Since the reference wave is a plane wave, it can be set to a constant $R(\xi, \eta) = R^*(\xi, \eta) = 1$. Equation 2.2 can be simplified to

$$R(\xi, \eta)h(\xi, \eta) = |O|^2 + 1 + O^* + O. \tag{2.13}$$

In in-line setup, the term $|O|^2 + 1$ is the DC term that serves as the background. O^* and O form a real image behind the hologram at z_0 and a virtual image in front of the hologram at $-z_0$, respectively, as shown in Fig. 2.2 (c). When one of the images gets focused, the other one gets focused as well. The two focused images are overlapping on the reconstructed plane, which is called the twin image problem. The twin image problem results in noise in the reconstruction process and it is significant when the particle density is high (Meng et al., 1993). Numerical suppression method (Denis et al., 2008) has been developed to weaken the

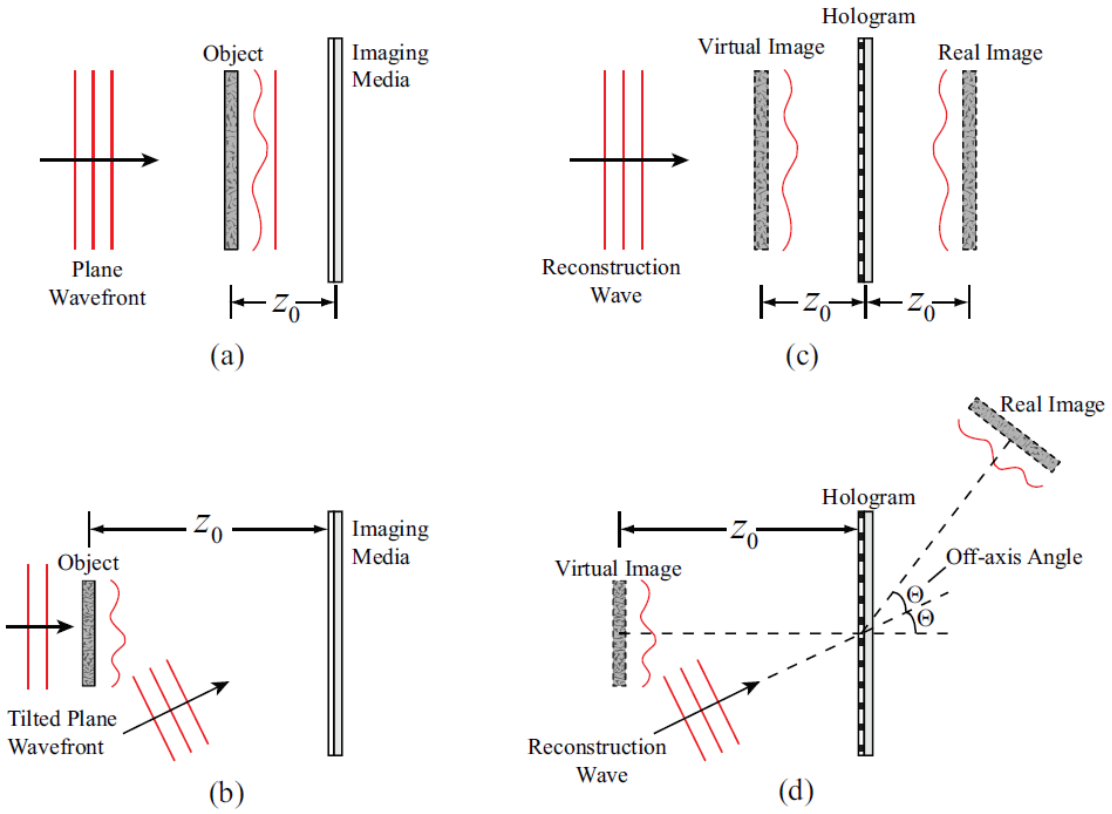

Figure 2.2. Schematics of in-line setup and off-axis setup of holography. (a) in-line recording process, (b) off-axis recording process, (c) in-line reconstruction process, (d) off-axis reconstruction process (Gao, 2014).

effect of the twin image problem. Also, in-line setup is simple to set up, which requires less equipment and less time to calibrate. The resolution requirement of the digital camera in in-line setup is lower than that of off-axis setup.

The twin image problem can be solved in the off-axis because of the tilt angle between the object wave and reference wave (θ), as shown in Fig. 2.2 (d). Assuming the angles between the direction of reference wave and x, y and z directions are θ_x, θ_y and θ_z, respectively. The reference wave can be mathematically expressed as

$$R(\xi,\eta) = \exp\left[j\left(\xi cos\theta_x + \eta cos\theta_y\right)\right]. \tag{2.14}$$

With this expression, the reconstruction process (Equation 2.13) can be written in

$$\begin{aligned} R(\xi,\eta)h(\xi,\eta) =& (|O|^2+1)\exp\left[j\left(\xi\cos\theta_x + \eta\cos\theta_y\right)\right] \\ &+ O^*\exp\left[2j\left(\xi\cos\theta_x + \eta\cos\theta_y\right)\right] + O. \end{aligned} \tag{2.15}$$

In this equation, the real and virtual images are formed by the last two terms respectively. Comparing to the in-line setup, the focused virtual image stays at the same position while the focused real image will shift by 2θ. As a result, the real image and virtual image can be separately observed, so the twin image problem can be eliminated. However, there are disadvantages of the off-axis setup. As mentioned above, the setup complexity of the off-axis setup is higher than the in-line setup. Also, the tilt angle (θ) has a maximum which needs to be determined while the requirements on the digital camera and laser are more strict than the in-line setup.

2.3 Digital Holography

In analog holography, the hologram plane is set in the middle of the object plane and reconstruction plane, as shown in Fig. 2.3. A chemically processed film is required to record the interference patterns of hologram, which should be able to scan in a range so that the reconstruction images with different reconstructed distance z can be obtained.

The introduction of digital imaging devices modifies this analog process into an easier one which is named as digital holography, where a digital camera records the hologram and stores

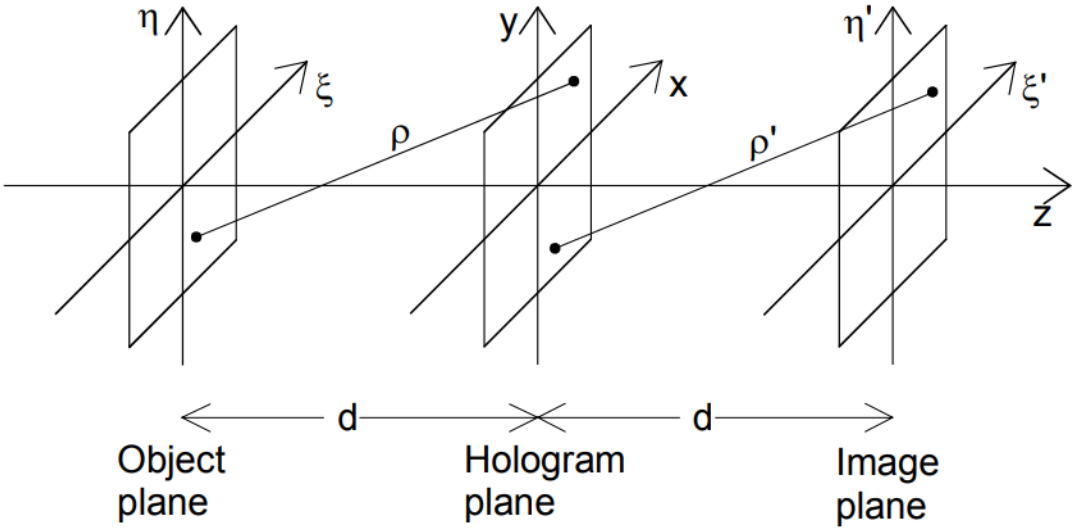

Figure 2.3. Analog holography process (Schnars and Jueptner, 2005).

it as a gray-scale image. As a result, the reconstruction process is numerically calculated by computer (Schnars and Jüptner, 1994) instead of setting up the reconstruction plane. In this process, the recorded hologram is discrete data, so the integral in Equation 2.3 is evaluated numerically and the refocusing process (Equation 2.11) is turned into a numerical evaluation. The physical scanning of the reconstruction plane in analog holography can be replaced by changing the value of reconstructed distance z in the reconstruction software. Also, imaging processing techniques can be applied to the process which can improve the performance of the digital reconstruction. The application of high-speed camera allows the recording of a dynamic process.

Charge-coupled device (CCD) and complementary metal-oxide-semiconductor (CMOS) cameras are commonly used for digital holography. The most important parameter for digital cameras in digital holography is the sensor size, which includes the pixel number and pixel size. The pixel number is the number of pixels in CCD or CMOS sensors. The larger pixel number, the larger field of view can be recorded. The pixel size is the center-to-center length between two neighbor pixels when assuming each pixel is in square shape. The pixel size refers to the resolution of the image recorded by the camera. CCD cameras usually have a smaller pixel size ($\sim 7\mu m$) compared to CMOS cameras ($\sim 20\mu m$). So when the object is small, more pixels are used to describe the object in CCD cameras so that the images recorded by CCD camera can show more detailed morphology. On the other hand, CMOS cameras perform better in saving and transferring data at a very high frame rate. As a result, CMOS cameras are suitable to record a transient or unsteady process.

With the digital camera, the analog image of the hologram is replaced by a digital grey-scale image. The intensity of each pixel is represented by the average intensity within the pixel square of the digital camera. The digital hologram is stored as a 2D matrix $h(m, n)$ in computer. Each element in the matrix represents the intensity at the corresponding planar position of the hologram. This matrix is used as the hologram part $h(\xi, \eta)$ in Equation 2.3.

However, Equation 2.3 is too complicated to convert to a discrete version. With a paraxial approximation (Goodman, 2005), Fresnel Approximation is the first method used to simplify Equation 2.3:

$$E(x,y,z) = \iint_{-\infty}^{+\infty} h(\xi,\eta)R^*(\xi,\eta)\frac{\exp(jkz)}{jz\lambda}\exp\left\{\frac{jk}{2z}\left[(x-\xi)^2+(y-\eta)^2\right]\right\}d\xi d\eta. \quad (2.16)$$

Fresnel approximation requires that the reconstructed distance z is large enough and the criterion can be mathematically expressed as (Schnars and Jueptner, 2005)

$$z >> \sqrt[3]{\frac{1}{8}\frac{[(x-\xi)^2+(y-\eta)^2]^2}{\lambda}}. \quad (2.17)$$

To eliminate the double integral in Equation 2.16, Fourier Transform is applied:

$$E(x,y,z) = \frac{\exp(jkz)}{jkz}\exp(j\frac{k}{2z}(x^2+y^2))\mathcal{F}\left\{h(\xi,\eta)R^*(\xi,\eta)\exp\left(j\frac{k}{2z}(\xi^2+\eta^2)\right)\right\} \quad (2.18)$$

Then, Equation 2.18 is converted to discrete version by substituting the digital hologram,

$$\begin{aligned} E(p,q,z) =& \frac{\exp(jkz)}{jkz}\exp\left(j\frac{k}{2z}\left[(p\Delta x)^2+(q\Delta y)^2\right]\right) \\ & FFT\left\{h(m,n)R^*(m,n)\exp\left(j\frac{k}{2z}\left[(m\Delta\xi)^2+(n\Delta\eta)^2\right]\right)\right\}, \end{aligned} \quad (2.19)$$

where FFT refers to fast Fourier transform which is a commonly used discrete Fourier Transform algorithm. Δx and Δy are the size of a pixel in the reconstructed image in x and y directions. $\Delta\xi$ and $\Delta\eta$ are the pixel size in the horizontal and vertical direction of the camera, respectively. In this simplification, Δx and Δy are dependent on the reconstruction distance z by

$$\Delta x = \frac{\lambda M\Delta\xi}{z}, \qquad \Delta y = \frac{\lambda N\Delta\eta}{z}, \quad (2.20)$$

where M and N are the pixel numbers of the camera in the ξ and η directions. This dependence is harmful to the reconstruction process because the reconstructed images at different reconstruction distances have different sizes. Rescaling is needed to get these images to the same size which is necessary for further particle detection process (Zhang et al., 2004).

To get rid of the disadvantage of rescaling which results from the discretization process in Equation 2.19, the double integral in Equation 2.16 can be rewritten with convolution operation as

$$E(x,y,z) = \{h(\xi,\eta)R^*(\xi,\eta)\}\otimes g'(\xi,\eta,z), \quad (2.21)$$

where $g'(\xi, \eta, z)$ is the Fresnel diffraction kernel (Gao, 2014):

$$g'(\xi, \eta, z) = \frac{\exp(jkz)}{jz\lambda} \exp\left[\frac{jk}{2z}(\xi^2 + \eta^2)\right]. \tag{2.22}$$

One is noted that the Fresnel diffraction kernel $g'(\xi, \eta, z)$ has an analytical expression in Fourier Transform,

$$G'(f_x, f_y, z) = \mathcal{F}\{'(\xi, \eta, z)\} = \exp(jkz) \exp\left[-j\pi\lambda z({f_x}^2 + {f_y}^2)\right]. \tag{2.23}$$

With the discretization of Equation 2.21 and discrete Fourier Transform, the equation can be rewritten as

$$E(p, q, z) = exp(jkz) FFT^{-1}\left\{FFT\{h(m, n)R^*(m, n)\} \exp\left\{-j\pi z\lambda\left[(\tfrac{m'}{M\Delta\xi})^2 + (\tfrac{n'}{N\Delta\eta})^2\right]\right\}\right\}, \tag{2.24}$$

where FFT^{-1} refers to the inverse fast Fourier Transform, m' and n' denotes the horizontal and vertical discrete position in frequency domain, respectively. With inverse discrete Fourier Transform, the complex amplitude in reconstructed image $E(p, q, z)$ is in spatial domain, which means the pixel size of the reconstructed image always equals to the pixel size of the camera. This simplification method is named as Convolution Approach (Schnars and Jueptner, 2005). Because the simplification is based on the Fresnel approximation (Equation 2.16), it still need to satisfy the criterion as illustrated in Equation 2.17.

Instead of using the Fresnel approximation, the simplification process can be started from the convolution expression of the Rayleigh-Sommerfeld diffraction equation as shown in Equation 2.6. The Fourier transform of the Rayleigh-Sommerfeld diffraction kernel mentioned in Equation 2.7 also have an analytical expression as shown in Equation 2.7. With the similar procedures in Convolution Approach, the discrete form of the complex amplitude in the reconstructed image is written as

$$E(p, q, z) = FFT^{-1}\left\{FFT\{h(m, n)R^*(m, n)\} \exp\left[jkz\sqrt{1 - (\frac{m'\lambda}{M\Delta\xi})^2 - (\frac{n'\lambda}{N\Delta\eta})^2}\right]\right\}. \tag{2.25}$$

This simplification is named as angular spectrum method (Katz and Sheng, 2010), which also uses inverse discrete Fourier Transform to convert the complex amplitude $E(p, q, z)$

into the spatial domain. So it does not have the problem with rescaling. Besides, this simplification gets rid of using Fresnel approximation so that it does not need to satisfy the requirement of reconstruction distance. The angular spectrum method can be applied when the object is close to the digital camera.

Alternatively, there is another method to perform reconstruction called wavelet transform. It uses the wavelet representation to simplify the double integral in Equation 2.3 in a discrete form. The wavelet representation is defined as (Buraga-Lefebvre et al., 2000)

$$\begin{aligned} WT(m,n,z) =& \frac{\pi}{z\lambda}\left\{\sin[\pi\frac{(m\Delta\xi)^2+(n\Delta\eta)^2}{z\lambda}] - \frac{\sin(\arctan(\sigma^2))}{\sqrt{1+\sigma^4}}\right\} \\ & \exp\left[\pi\frac{(m\Delta\xi)^2+(n\Delta\eta)^2}{z\lambda}\frac{1}{\sigma^2}\right], \end{aligned} \tag{2.26}$$

where $WT(m,n,z)$ is the wavelet representation and σ^2 is called the size of the wavelet. This number is determined by the image size. By testing with enough hologram samples, the size of wavelet is expressed as

$$\sigma^2 = 3\frac{0.6822}{4z\lambda}\min[(M\Delta\xi)^2,(N\Delta\eta)^2], \tag{2.27}$$

With the wavelet representation defined by Equation 2.26, the complex amplitude of the reconstructed image can be written as

$$E(p,q,z) = FFT^{-1}\left\{FFT\left\{h(m,n)R^*(m,n)\right\}FFT\left\{WT(m,n,z)\right\}\right\} \tag{2.28}$$

The performance of the wavelet transform method is based on accuracy of the size of wavelet σ^2. The failure of determining the accurate size of wavelet will lead to defocus of the reconstructed image. To get a more accurate size of wavelet, a wavelet family is usually created (Lebrun et al., 1999).

In general, with the application of digital cameras and numerical reconstruction methods, digital holography simplifies the experimental setup and accelerate of the reconstruction process compared to the analog holography. However, digital cameras usually have a larger pixel size compared to analog image film. A common used CCD has a pixel size of several microns while the pixel size of an analog image film can be less much than $1\mu m$. This problem affects the digital holography in two ways. Firstly, the digital images lose detailed

morphology of the object because fewer pixels are used to describe the object, especially for small objects. It cannot detect objects which are smaller than the pixel size of the digital camera. For example, for a $4\mu m$ diameter particle, the CCD camera may not able to record the particle while the analog film can describe the particle with more than 4×4 pixels. The second effect of the large pixel size is on the setup of off-axis holography. In the off-axis setup, there is an angle between the object light and reference light. This angle θ has to satisfy a criterion (Schnars and Jueptner, 2005)

$$\theta < \frac{\lambda}{2\Delta\xi}, \tag{2.29}$$

where each pixel is assumed in square shape. i.e. $\Delta\xi = \Delta\eta$. For an analog film with $0.5\mu m$ pixel size and $532nm$ light source, the angle between the object and the reference light can get to $30.5°$. But this angle decreases to $2°$ when a CCD camera with $7.4\mu m$ pixel size is used. From this aspect, digital holography should use in-line setup or very small angle off-axis setup.

2.4 Digital In-line Holography

A typical digital in-line holography (DIH) process is shown as Fig. 2.4. In the recording process, a plane wave illuminates the particle field and the scattered light serves as the object wave. The reference wave comes from the undisturbed part of the plane wave. The interference pattern between the object wave and reference wave is recorded by the imaging sensor which is the recorded in-line hologram $h(m, n)$ as shown in Fig. 2.4 (a) . The hologram is then reconstructed at different z position and the information of the 3D position and size of the particles can be extracted from the reconstructed images as shown in Fig. 2.4 (b). In the reconstruction process, the reference beam used here is a plane wave which is uniform in the plane, which can be assumed as

$$R^*(m, n) = R(m, n) = 1. \tag{2.30}$$

By applying this attribute to the aforementioned reconstruction methods (Equations 2.19, 2.24, 2.25 and 2.28), the complex amplitude of the reconstructed images can be evaluated.

The particles in the reconstructed planes are well-focus when the reconstruction distance z equals to the distance between the particle in the field and the hologram plane.

2.5 Applications of Digital Holography

In the beginning, analog holograph is applied to measure the particle size and 3D velocity of tracing particles in turbulent flows (Tao et al., 2000). Digital holography is invented by introducing the computers and has been applied to a variety of areas including flow measurements (Sheng et al., 2008), diagnostics of the droplets breakup (Guildenbecher et al., 2014) and spray (Lü et al., 2009; Yang and Kang, 2011). In addition, with a digital holographic microscopy (DHM) system can be set up which decreases the extended depth of focus (EDOF). The DHM system has been applied to the biological study such as the behavior of microorganism (Sheng et al., 2007; Lee et al., 2011) and aquatic animals (Gao, 2014). DHM has also been applied to the measurements of the flow in a turbulent boundary layer (Sheng et al., 2008), the diagnostics of the spray structure of aerated jet (Lee et al., 2009) and aerodynamics of the drop breakup of non-Newtonian fluid (Gao, 2014). A double-exposure DIH system is applied to characterized the spray field created by a nozzle (Yang and Kang, 2011). In addition, the DH system is applied to measure the particles in a supersonic jet flow (Buchmann et al., 2012) and the shotgun pellets or projectiles(Guildenbecher et al., 2013b). The size distribution and concentration of burning pulverized coal particle can be measured with DH after eliminating the effect from flame (Wu et al., 2017).

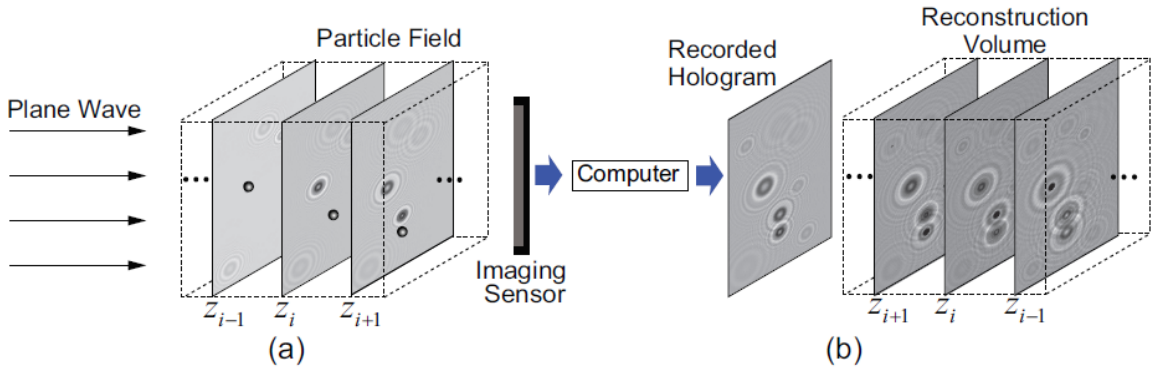

Figure 2.4. Schematic of DIH for the measurement of a particle field.(a) recording and (b) reconstruction (Gao et al., 2013).

3. HOLOGRAPHY-BASED PARTICLE DETECTION METHODS

Holography can be applied to record the 3D images of particle fields. By reconstructing the recorded holograms, the 3D positions and sizes of different particles can be identified. This is usually achieved by extracting the in-plane $(x-y)$ position and the size of every individual particle, followed by analyzing the depth. Among them, identifying the z-position is a key challenge. From the reconstructed complex amplitude at depth z, $E(p,q,z)$, one can get the corresponding intensity, $I(p,q,z) = E(p,q,z)\cdot E^*(p,q,z)$. By examining the change of I at different reconstructed locations, different methods can be referred to detect the particle location. A brief summary of the particle detection methods is presented here.

3.1 Laplacian Method

The Laplacian (LAP) method (Choi and Lee, 2009) introduces a new variable , LAP value, to help locate the depth of a particle.

$$LAP(z) = \sum_{p,q\in W} \left[\nabla^2 \left(I(p,q,z)\right)\right]^2 . \tag{3.1}$$

Here, $\nabla^2(I(p,q,z)) = [I(p+1,q,z)+I(p-1,q,z)+I(p,q+1,z)+I(p,q-1,z)- 4I(p,q,z)]$, which is the spatial gradient of a pixel. The depth of the particle is located at where $LAP(z)$ reaches maximum, i.e., $z_0 = arg\ max[LAP(z)]$.

The LAP method is used to measure the 3D motion of red blood cells with digital holographic microscopy (Choi and Lee, 2009). However, the accuracy of the LAP method is low because the spatial gradient of the intensity of a point is determined only by its 4 neighbor points.

3.2 Correlation Coefficient Method

The Correlation Coefficient (CC) method (Yang et al., 2008) determines the depth of a particle by examining the correlation coefficient between two adjacent reconstructed planes.

$$CC(z) = \frac{\sum_{p,q \in W} [(I(p,q,z) - \bar{I}_W(z))(I(p,q,z+\Delta z) - \bar{I}_W(z+\Delta z))]}{\sqrt{[\sum_{p,q \in W} (I(p,q,z) - \bar{I}_W(z))^2][\sum_{p,q \in W} (I(p,q,z+\Delta z) - \bar{I}_W(z+\Delta z))^2]}}, \tag{3.2}$$

where z and $z + \Delta z$ are the reconstruction distance of two adjacent reconstructed planes. $\bar{I}_W(z)$ is the mean intensity averaged in the reconstructed window W. The depth of the particle is determined by maximizing $CC(z)$, i.e., $z_0 = arg\ max[CC(z) + \frac{\Delta z}{2}]$.

The CC method is only tested with synthetic holograms. It is found that the accuracy of the method highly depends on the distance between adjacent reconstructed planes, Δz. If Δz is large, the resolution of depth is low. However, if Δz is small, the method is very sensitive to noise because $CC(z)$ changes slightly when it gets close to the focal plane.

3.3 Variance Method

The Variance (VAR) method (Palero et al., 2007; Darakis et al., 2010) determines the depth of a particle by analyzing the variance of the image intensity within the particle. When a particle is well focused in a digital image, the intensity distributed inside of the particle should be uniform. To implement the principle, the variance of image intensity inside of the particle expressed as

$$VAR(z) = \frac{1}{N} \sum_{p,q \in P} \left[I(p,q,z) - \bar{I}_P(z) \right]^2, \tag{3.3}$$

where P denotes to the pixels inside of the particle (including the edge), N is the number of the pixels of P, and $\bar{I}_P(z)$ is the mean intensity of P. The depth of the particle is then determined by minimizing the value of $VAR(z)$, i.e. $z_0 = arg\ min[VAR(z)]$.

The method is applied to the analysis of 3D positions and sizes of micro-droplets (Palero et al., 2007). However, the challenge of the method is to identify the pixels inside of the particle. In the existing method, A user-defined threshold is used to obtain the binary map from the intensity of the image, and the pixels inside the particle can be extracted from

the binary map. Therefore, the accuracy of the method depends on the threshold. If the user-defined threshold is not accurate, the depth of the particle has large error.

3.4 Minimum Intensity Method

The Minimum Intensity (MI) method (Khanam et al., 2011) determines the depth of a particle by analyzing average intensity inside of the particle image, which is expressed as

$$\bar{I}(z) = \frac{1}{N} \sum_{p,q \in P} I(p, q, z), \tag{3.4}$$

where P is the pixels inside of the particle, and N is the number of the pixels of P. The depth of the particle is determined by minimizing the average intensity inside the particle, i.e., $z_0 = arg\ min[\bar{I}(z)]$. The MI method is applied to determine the sizes of needle-shaped particles (Khanam et al., 2011). This method processes very fast because the expression in Equation 3.4 is simple. However, this method has relatively high errors in determining the depth position of the particle. Also, this method faces the same challenge as the VAR method.

3.5 Minimum Edge Intensity Method

The Minimum Edge Intensity (MEI) method (Tian et al., 2010) determines the depth position by averaging the depth of edge pixels, i.e.,

$$z_0 = \frac{1}{N_{Edge}} \sum_{p,q \in Edge} z_m(p, q), \tag{3.5}$$

where $z_m(p, q)$ denotes the depth corresponding to the minimum intensity of every individual edge pixels, i.e., $z_m(p, q) = arg\ min\,[I(p, q, z)]$. N_{Edge} is the number of the particle edge pixels.

The MEI method is applied to measure the 3D positions and sizes of bubbles in fluid flow because the edge pixels of bubbles are easy to identify in digital image. However, the challenge of identifying edge pixels becomes significant when it is applied to other kinds of

particle. Failure to identifying the correct pixels of particle edge leads to large errors in determining the depth position of the particle.

3.6 The HYBRID Method

The HYBRID method is based on the analysis of the reconstructed images. It combines the information of the minimum intensity and the maximum edge sharpness. The edge pixels are determined by a minimum intensity map I_m and a maximum Tenengrad map T_m which are expressed as (Gao et al., 2013)

$$I_m(p,q) = \min_{z_{min} \le z \le z_{max}} I(p,q,z), \tag{3.6}$$

$$T_m(p,q) = \max_{z_{min} \le z \le z_{max}} T(p,q,z), \tag{3.7}$$

where $I(p,q,z)$ is the intensity of a reconstructed image at distance z. The relationship between the intensity and the complex amplitude $E(p,q,z)$ is

$$I(p,q,z) = |E(p,q,z)|^2, \tag{3.8}$$

The Tenengrad operator $T(p,q,z)$ is the sharpness of a pixel in the reconstructed image, which is expressed as (Tenenbaum, 1970)

$$T(p,q,z) = [A(p,q,z) \otimes S_x]^2 + [A(p,q,z) \otimes S_y]^2, \tag{3.9}$$

Where A(p,q,z) refers to the amplitude image which is defined as

$$A(p,q,z) = |E(p,q,z)|, \tag{3.10}$$

And S_x and S_y are called the horizontal and vertical Sobel kernels

$$S_x = \frac{1}{4}\begin{bmatrix} -1 & 0 & 1 \\ -2 & 0 & 2 \\ -1 & 0 & 1 \end{bmatrix}, \qquad S_y = \frac{1}{4}\begin{bmatrix} 1 & 2 & 1 \\ 0 & 0 & 0 \\ -1 & -2 & -1 \end{bmatrix}. \tag{3.11}$$

The distance range z_{min} and z_{max} for the reconstruction is defined by the the estimation of the depth of the particle field. Usually the interval between two consecutive reconstruction

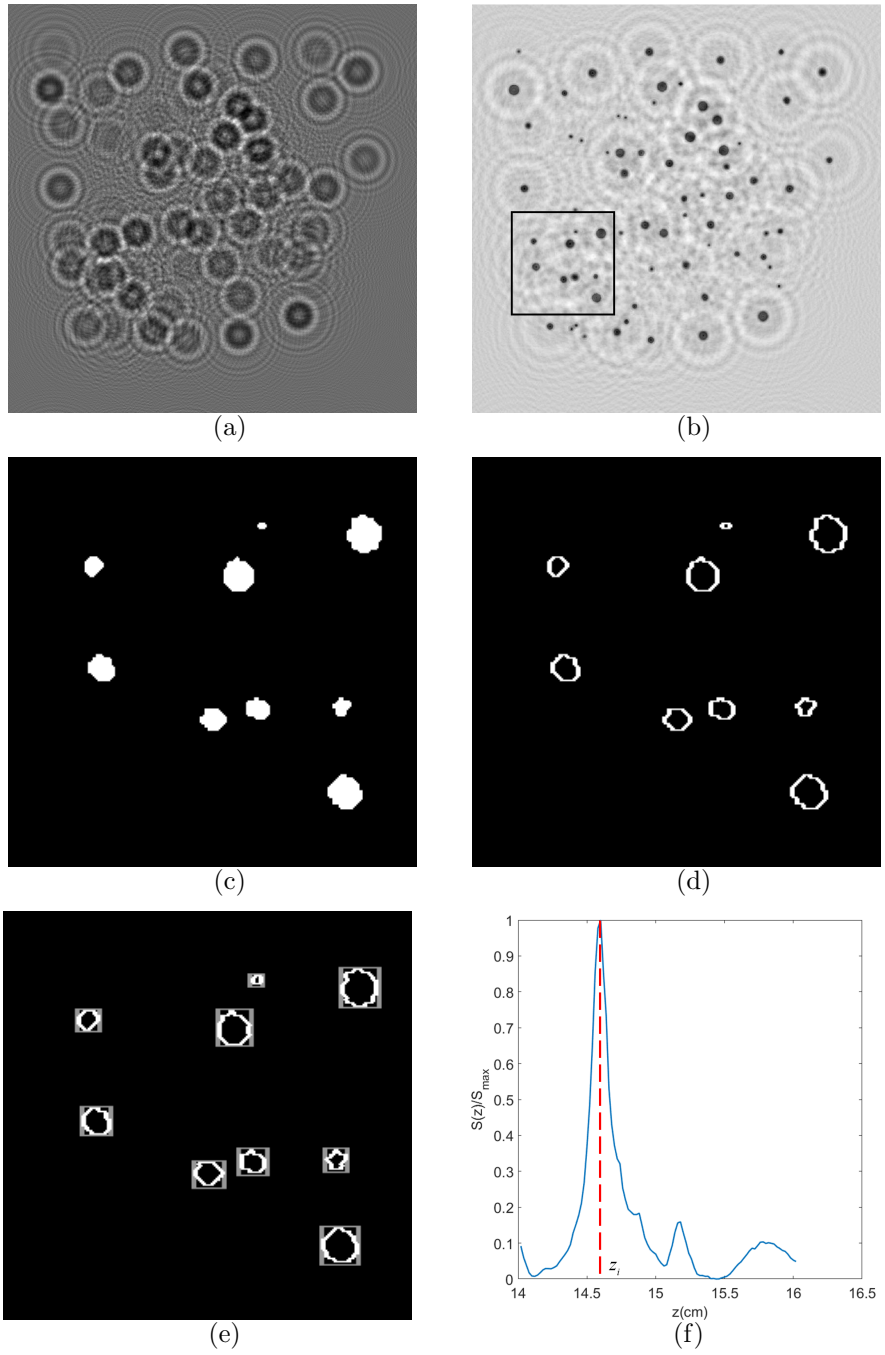

Figure 3.1. Procedures of HYBRID method: (a) synthetic hologram $h(m, n)$, (b) minimum intensity map $I_m(p, q)$, (c) binary image after thresholding operation, (d) edge identified map, (e) window created to separate particles, and (f) local sharpness $S_W(z)$ profile of the particle at upper right corner in (c) and maximum at z_i. (Only the square region in (b) is shown in (c), (d) and (e).)

plane is less than 100 μm so its effect on the accuracy is negligible. A sample of synthetic hologram is shown in Fig. 3.1 (a). The minimum intensity map from Equation 3.6 in shown in in Fig. 3.1 (b). The black regions in the minimum intensity map are the planar position of the particles. With a proper threshold and thresholding operation, the minimum intensity map can be transfer to a binary image which shows the exact edge of the particles as shown in Fig 3.1 (c). To make the figure clear, only the square region in Fig. 3.1 (b) is shown. For the convenience of further process, the image is inverted so that the background turned to black and the particles are white. From this binary image, the edge for each particle can be extracted as Fig. 3.1 (d) shown. The edge of the particles is exact only if the threshold is accurate. Previously, the threshold is defined by the user so it may not be accurate, especially when the user is lack of experience. The HYBRID method searches for the threshold automatically, which increases the accuracy of the edge determination. The threshold searching process introduces a new parameter, edge sharpness (Gao et al., 2013),

$$S(t) = \frac{\sum_{p,q}(\mathcal{E}\{\mathcal{T}_t\{I_m\}\} \cdot T_m)}{\sum_{p,q}\mathcal{E}\{\mathcal{T}_t\{I_m\}\}}. \tag{3.12}$$

I_m and T_m are the minimum intensity map and the maximum Tenengrad map as mentioned above. $\mathcal{T}_t\{\}$ refers to the thresholding operation with the threshold t, which is to binarize the image by assigning "0" to the pixels whose values are greater than t while assigning "1" to the rest pixels. This operation includes inverting of the image. The symbol $\mathcal{E}\{\}$ is the operation to find the edge of the binary segments which zeros the value of the pixels whose value is "1" but the surrounding pixels value are all "1". As a result, Equation 3.12 represents the fraction of the total edge sharpness of the image over the number of edge pixels, so it is the average edge sharpness of the image. The threshold is optimized to t_0 when the edge sharpness peaks, i.e., $t_0 = arg\ max\{S(t)\}$. To search for the optimal threshold t_0, a range for searching is need from t_{min} to t_{max}. For the easiness of determining the searching range, the minimum intensity map I_m is normalized by

$$I_{m,normalized}(p,q) = \frac{I_m(p,q)}{\max_{p,q}\{I_m(p,q)\}}, \tag{3.13}$$

The values in the normalized map ranges from 0 to 1 so the range for searching threshold can be set to $[t_{min}, t_{max}] = [0, 1]$.

With the particle edges identified, the in-plane $(x-y)$ position and the size of the particles can be determined. The particles are small enough so that they are assumed to be spherical. The four points at the top, bottom, left and right respectively are used to determine the position of the center point of the particle , which mathematically expressed as

$$\begin{aligned} X_{center} &= \frac{\max\limits_{p,q\in Edge}\{p\} + \min\limits_{p,q\in Edge}\{p\}}{2}, \\ Y_{center} &= \frac{\max\limits_{p,q\in Edge}\{q\} + \min\limits_{p,q\in Edge}\{q\}}{2}. \end{aligned} \tag{3.14}$$

The size of the particle is determined as equivalent circle diameter. With the convex hull algorithm, the pixels at the edge are connected into a polygon and equivalent circle diameter of this polygon is used as the size of the particle, i.e.,

$$D_{eq} = \sqrt{\frac{4A_p}{\pi}}, \tag{3.15}$$

where A_p denotes the area spanned by the detected edge.

After the 2D morphology information is determined, the depth of each particle is calculated. The particles in the particle field need to be separated first and then out-of-plane z position of each of the particle are determined. Rectangular windows are created to separate the particles. Each window encloses an individual particle and the z position is analyzed in a local window as shown in Fig. 3.1 (e). To make sure the edge is identified accurately, the threshold optimization process is repeated for each window and get a local optimized threshold $t_{0,i}$, where i is the index of the ith window, obtained by the maximum of the local edge sharpness, which is expressed as

$$\begin{aligned} S_W(t) &= \frac{\sum\limits_{p,q\in W}\left(\mathcal{E}\left\{\mathcal{T}_t\left\{I_m\right\}\right\}\cdot T_m\right)}{\sum\limits_{p,q\in W}\mathcal{E}\left\{\mathcal{T}_t\left\{I_m\right\}\right\}}, \\ t_{0,i} &= arg\ max\left\{S_W(t)\right\}, \end{aligned} \tag{3.16}$$

During this process, to make sure the true edge is enclosed in the window, the window needs to be expanded by a factor. With this new local optimized threshold, the edge sharpnesses,

$S_W(z)$ at all reconstruction distance z in the reconstruction distance range $[z_{min}, z_{max}]$ are calculated for the same window which is expressed as

$$S_W(z) = \frac{\sum_{p,q \in W} \left(\mathcal{E}\left\{\mathcal{T}_{t_{0,i}}\left\{I(p,q,z)\right\}\right\} \cdot T(p,q,z)\right)}{\sum_{p,q \in W} \mathcal{E}\left\{\mathcal{T}_{t_{0,i}}\left\{I(p,q,z)\right\}\right\}}. \tag{3.17}$$

By maximizing the edge sharpness for all reconstruction distance in a single window, $S_W(z)$, the depth location in z-direction of the particle enclosed by the window is determined. i.e., $z_i = arg\ max\left\{S_W(z)\right\}$, as shown in Fig. 3.1 (f). By repeating this process for all the windows created, the position of all particles can be determined. To improve the edge calculation accuracy, the threshold optimization process can be repeated at different reconstruction distance z and the optimal threshold at a reconstruction image in a window, $t'_{0,i}(z)$, is acquired to find a new edge.

Until now, there is an assumption made that every window enclose a single particle. However, the particles may overlap in the $(x-y)$ plane as shown in Fig. 3.2. Especially when the number of particles increases in the particle field. As a result, the detected edges of the two particles are connected as shown in Fig. 3.2 (b) and only one window is created to enclose the two particles. These two particles in one window are detected as one particle which is called false identification (Tian et al., 2010; El Mallahi and Dubois, 2013). This leads to an inaccurate analysis of the position and size of the enclosed particles. Different methods have been developed in the computer vision community to separate multiple particles in a single window (El Mallahi and Dubois, 2013). However, these methods focus on separating overlapping particles whose distances to the camera are close to each other. In contrast, in DIH applications, the overlapping particles are often lying on different distance z. The Refinement process is developed to solve this problem, which is used as a complement of the HYBRID method (Gao et al., 2014).

The refinement process aims at defining false particles and separating false particles. A false particle is defined as an incorrect identified particle which contains more than one particle actually (Gao et al., 2014). This definition includes, but not limited to, the overlapping particles as shown in Fig. 3.2. It also includes the redundant edge pixels from other particles in the window, which is caused by expanding the window as shown in Fig. 3.3.

(a)

(b)

Figure 3.2. Overlapping particles in $(x - y)$ plane: (a) binary image (Gao et al., 2014) (b) identified edge.

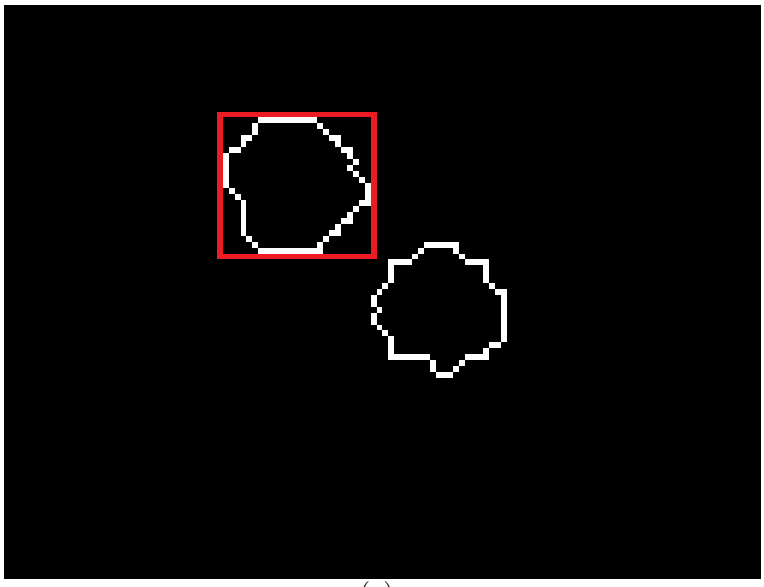

(a)

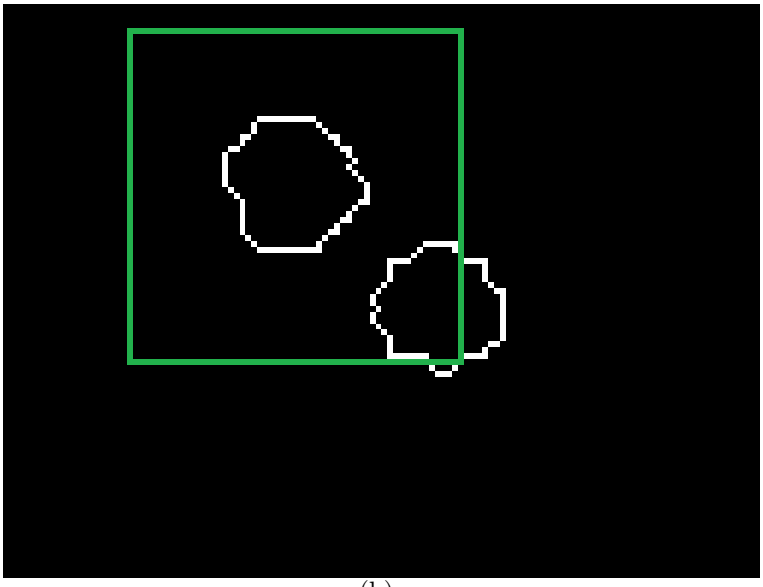

(b)

Figure 3.3. Illustration of false particles result from expanding window: (a) origin window (b) expanded window.

As mentioned above, the HYBRID method determines the out-of-plane z position (depth) by searching for the maximum of the local sharpness profile $S_W(z)$. The refinement process analyzes the peaks in the $S_W(z)$ profile in detail to identify the false particle and make correction to the calculation of the 3D position and size of the particles. In HYBRID method, the threshold is recalculated in each reconstructed plane in each window which is $t'_{0,i}(z)$. So Equation 3.17 can be written as

$$S_W(z) = \frac{\sum_{p,q \in W} \left(\mathcal{E}\left\{ \mathcal{T}_{t_{0,i}(z)} \left\{ I(p,q,z) \right\} \right\} \cdot T(p,q,z) \right)}{\sum_{p,q \in W} \mathcal{E}\left\{ \mathcal{T}_{t_{0,i}(z)} \left\{ I(p,q,z) \right\} \right\}}. \tag{3.18}$$

With Equation 3.18 the edge sharpness profile $S_W(z)$ of the particle in the window shown in Fig. 3.2 can be calculated and plotted as shown in Fig. 3.4, where more than one peaks can be identified. The two peaks in Fig. 3.4, t_A and t_B, correspond to the z positions of the two overlapping particles. With these two peaks, the edge pixels of the two particles in the window can be separate as shown in Fig. 3.5 (a) and (b). Then the in-plane $(x-y)$ position and size of the two particles can be determined by the separated edge pixels. The separated edge pixels are connected to a polygon with convex hull algorithm as shown in Fig. 3.5 (c) and (d), and the $(x-y)$ and size of the particles can be determined by Equation 3.15.

However, due to the noise in the hologram and false particle edge created by expanding window as shown in Fig. 3.3 (b). These peaks should not be considered as multiple particles in a single window. Some criteria should be applied to the refinement process. In the previous study, the peaks that meet the desired criteria are called valid peaks (Gao et al., 2014) which are considered as a particle. The height of the peak needs to be 60% or larger than the maximum value in the edge sharpness profile. Also, the width of the peak, quantified as the width above 80% of the peak value, needs to be less than 20 times the equivalent diameter of the particle, as shown in Fig. 3.4. The peak height requirement is to make sure all the edge pixels of the particle is enclosed in the window and to get rid of the occasion shown in Fig. 3.3 (b). In this occasion, the upper left corner of the outside particle is enclosed in the window by window expansion. The edge sharpness profile is plotted as Fig. 3.6 in which the peak in the circle is the valid peak denotes to the partial edge in the window in Fig. 3.3. This partial edge should not be considered as a valid particle in this window.

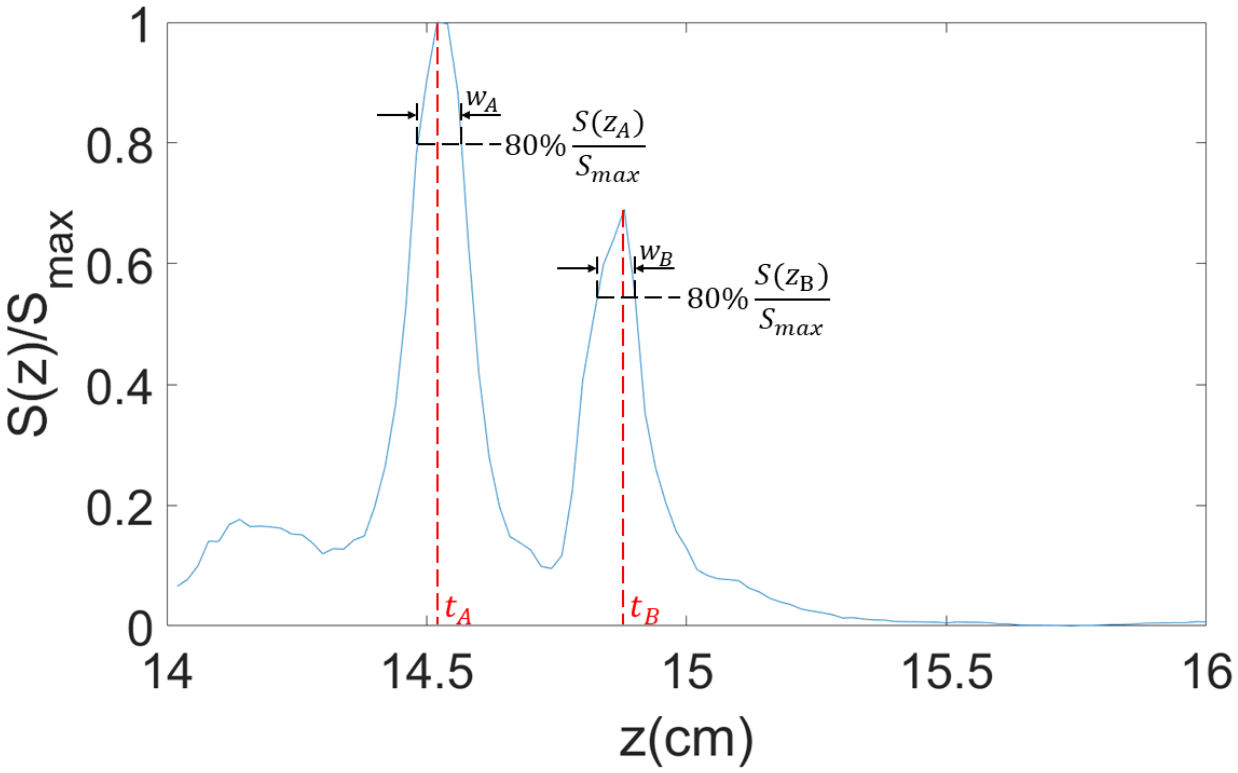

Figure 3.4. Edge sharpness profile of the false particle in Fig. 3.2 (b).

The requirement of the peak width is to ensure the edge of the particle being continuous. If the width of the peak is too large, the respective edge pixels comes from more than one particles. This means that there are multiple particles next to each other both in $x-y$ and z positions. In this situation, these closed-distributed particles cannot be identified by the HYBRID method.

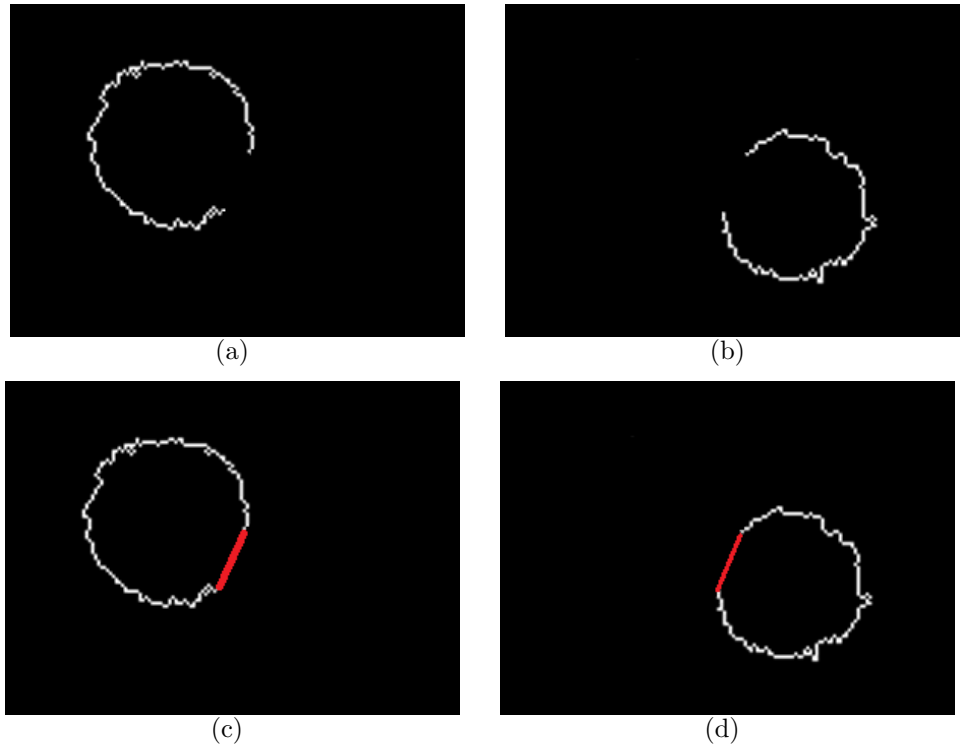

Figure 3.5. Separated edge pixels of the two particle from Fig. 3.2 (b) with refinement: (a), (b) separated edge. (c), (d) separated polygon by convex hull.

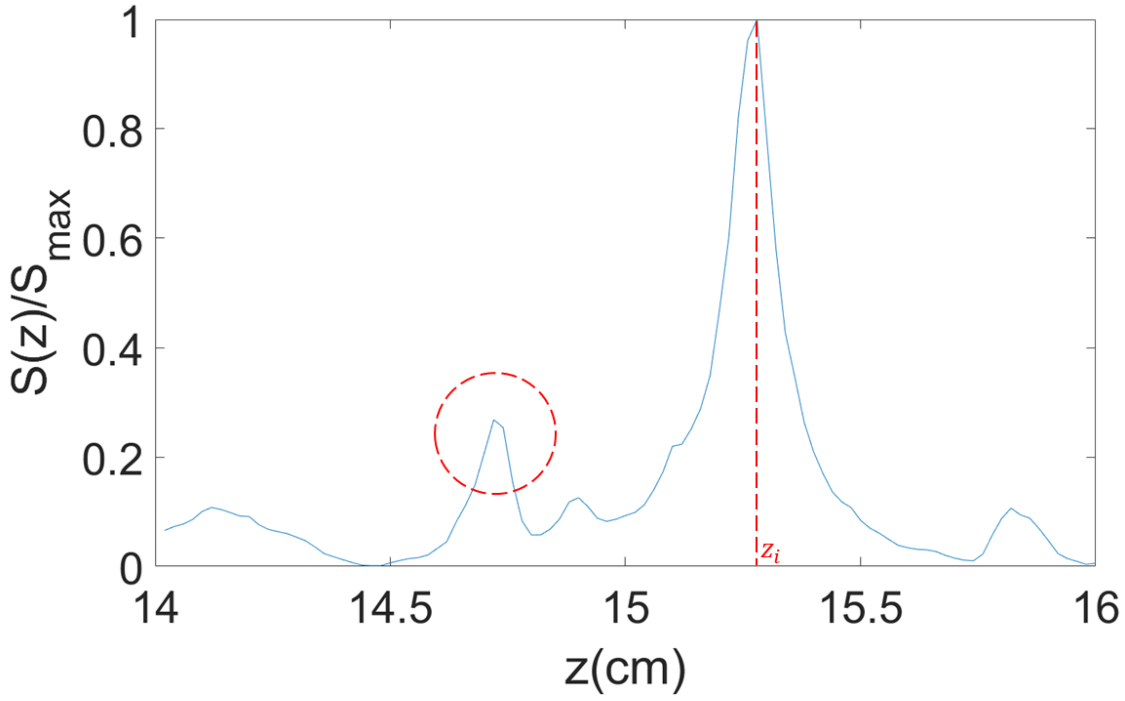

Figure 3.6. Edge sharpness profile calculated from the window in Fig. 3.3 (b). z_i denotes to the particle fully enclosed in the window and the peak in the circle is the invalid peak.

4. OBJECTIVES AND MOTIVATIONS

A software package is needed to digitally process the recorded hologram in digital holography for reconstruction and particle detection as a post-processing step. A variety of algorithms have been developed. However, they perform either slowly or less accurately because more repetitions and criteria are applied to the methods to reduce errors. In this study, starting from optimizing the HYBRID method with refinement (Gao et al., 2013). We aim at developing an accurate processing method for particle detection in digital holography. The optimization focuses on improving the time efficiency of the processing. Certain procedures in the HYBRID method are highly time-consuming but hardly improve the accuracy of the method. These procedures usually have redundant loops that can be removed in the optimization or be replaced by simpler alternatives.

Also, it is noticed that implementing the HYBRID algorithm involves a significant amount of loops. It is very suitable to adopt parallel processing algorithm, which helps to take advantage of the strong computing capacity of the multi-processor workstation or cluster. In this study, the message passing interface (MPI) algorithm is applied for parallel processing and the program runs on a remote workstation. The application of parallel processing increases the time efficiency significantly. To meet the requirement of the remote workstation, Python, a cross-platform programming language, is applied to code the processing algorithm.

The usefulness of the new method is tested in terms of both accuracy and time efficiency with synthetic holograms. The results of the new method are compared to the results of the existing HYBRID method with refinement. The comparison demonstrates how the optimization improves the time efficiency and how the modified method affects the accuracy.

Characterizing the solid particles is an important application of DIH. One is noted that, unlike spherical droplets or artificial particles, the natural solid particles always have irregular shapes. As a consequence, the morphology becomes a significant characteristic index of the particles. In this study, three kinds of natural solid particles are measured with a lensless

DIH system. The DIH system is applied to get focused images of the particles in a particle field. Equivalent diameter, circularity and aspect ratio are the three parameters introduced to quantify the irregular shapes, which is an implement of DIH to measure the solid particles. The statistics of the three parameters are used to describe the characteristics of the particles, which is further verified with the microscopic images of the solid particles.

5. DEVELOPMENT OF TIME EFFICIENCY OF PARTICLE DETECTION METHOD

5.1 Method

The interference patterns in a digital hologram encode the information of 3D position and size of particles. The processing methods is to decode these information from the recorded holograms. Processing the hologram includes two parts: digital reconstruction and particle detection. In digital reconstruction, the reconstructed wave fields at different planes can be evaluated numerically, and in particle detection, the multiple particles are firstly separated to determine their in-plane positions. Then the out-of-plane position and particle size are determined to each individual particle. To get accurate out-of-plane (z) position, the HYBRID method is developed, but it is very time-consuming. To speed up the process, several modifications are developed and parallel processing adopted. These modifications focus on reducing the complexity of the method while not affecting the accuracy. The parallel processing is aiming to speed up the process with powerful workstations or clusters.

5.1.1 Reduction of Time Consumption of Processing

A Matlab script has been developed to implement the HYBRID method and refinement process by Guildenbecher (Guildenbecher et al., 2013a). The reconstruction process can be improved with graphical processing units (GPU). However, this script is not fully developed in term of processing efficiency. In the present work, we try to improve the entire DIH, including the reconstruction and the particle detection.

In the present work, instead of Matlab, Python is selected as the coding platform for developing a more efficient software. With the advancement of the open source programming environment, Python provides thousands of user-community-defined modules in which fully developed morphology functions are steadily available. Most importantly, Python is a cross-platform programming environment. It works on different operating systems and it provides

interfaces to other programming languages so that the length of the script in Python can be reduced significantly. The object-orient programming (OOP) method is used to develop the Python script. The structure of the script can be developed into different objects to perform different functions of the HYBRID method and refinement process, as illustrated in Fig. 5.1, where each process is defined as an object in the script. By taking advantage of the OOP, the script is easy to read and flexible for modification. This easiness and flexibility are important for running the script on a remote cluster machine which usually has more computational resource. To run the Python code on a remote cluster, it is impossible to input the parameters manually. In this project, a folder named "image" is created. Users need to save all the images to be processed into this folder. A file named "parameter.txt" is also required to be upload into this folder. This file should include 4 numbers and 1 string which are separated with commas. The first and second number are the upper limit and lower limit for the reconstruction range in z-direction in millimeter, respectively. The third number is the number of reconstruction slides wanted. By increasing the number of reconstructed slides, the error of the out-of-plane z position will be reduced but the processing time will be increased at the same time. The fourth number is the pixel size of the image in micrometer which is used to calculate the in-plane position and particle size. The string is to specify the selected reconstruction method. It should be "Angular Spectrum", "Convolution" or "Wavelet". In this project, all images are reconstructed with the angular spectrum method.

After changing the programming language to Python, the complexity of several parts of the HYBRID method and refinement process is reduced. In the thresholding process, the HYBRID method optimizes the threshold for the minimum intensity map to find the in-plane $(x - y)$ position. After the enclosed windows are created, the threshold in each window on each reconstructed images are optimized again to get $t_i(z)$ where i stands for the number of windows and z denotes to the reconstruction distance. As a result, the threshold optimization process repeats for the number of windows multiplied by the number of reconstruction planes times, which is time-consuming. However, compared to this massive time consumption, the resultant improvement of the accuracy is limited. The purpose of

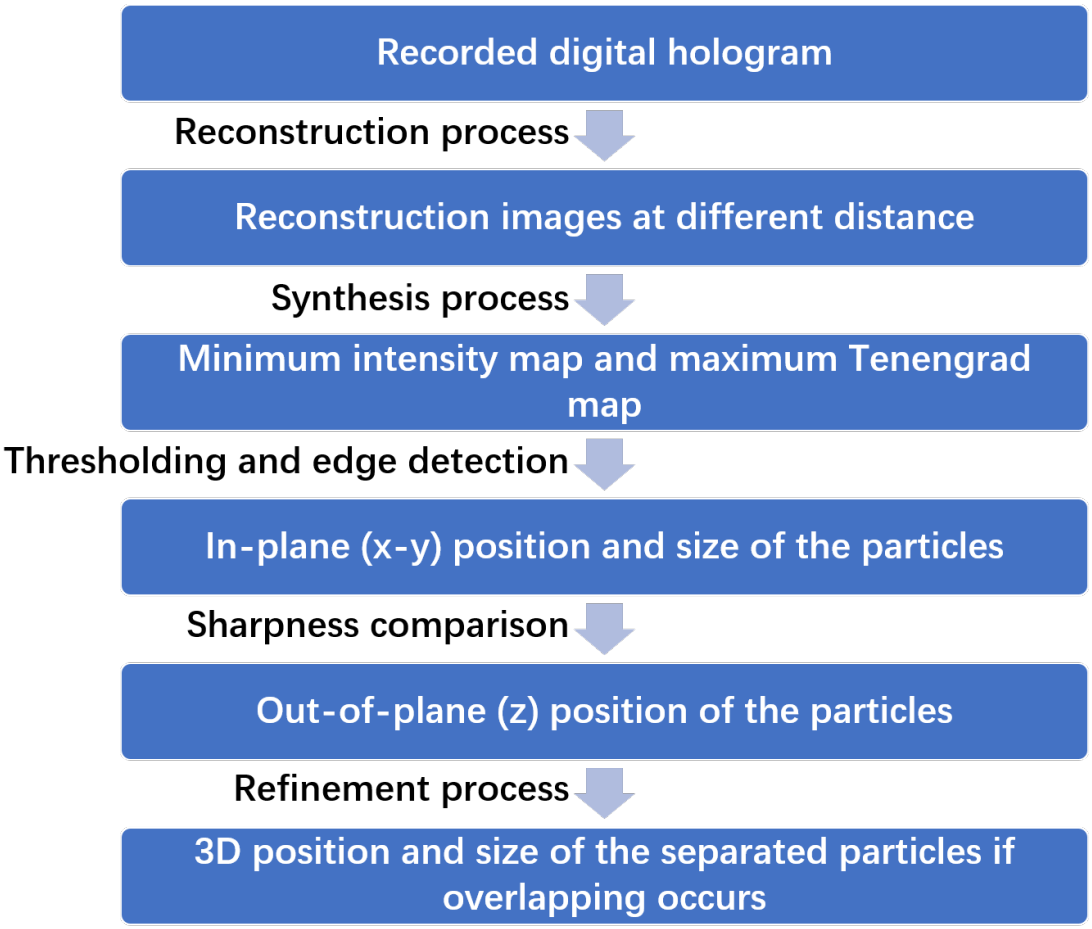

Figure 5.1. Illustration of the object-oriented programming (OOP) of the HYBRID method and refinement process.

threshold optimization is to improve the accuracy of edge pixels determination. As Equation 2.11 demonstrates, only when the reconstruction distance z equals to the object distance z_0, the particle in a given window is in-focus in the image. Thus, only at the reconstructed image of $z = z_0$, the edge pixels of the particle is accurate by threshold optimization. In contrast, in other reconstructed images, the particle is out-of-focus so that no matter what value of the threshold is used, the edge pixels of the particle are inaccurate. This means the threshold optimization process for all the reconstruction planes except for the true value one are invalid. In addition, by comparing the local optimized threshold at each reconstructed plane $t'_{0,i}(z)$, there is a relatively large range of threshold to give the accurate edge pixels. Based on these finding, the optimization of the threshold at each reconstructed plane is canceled. Instead, the local optimized threshold $t_{0,i}$ calculated from Equation 3.16 is used to calculate edge sharpness and plot for the edge sharpness profile. Based on this profile, the valid peaks are found with the same refinement process as described in section 3.6 and the corresponding distances $z_{d,i}$ are obtained. The threshold optimization process is only repeated in the window of a reconstructed plane at $z = z_{d,i}$. Then by repeating the process of searching for peaks in the edge sharpness profile, more accurate distances of the particles are obtained as $z'_{d,i}$ which is the out-of-plane position of the particles. Definitely, this process can be repeated more times to get a more accurate result, like a recursion, until the result is accurate enough. However, by increasing the times of repeating the process, the processing time will increase exponentially, which is undesirable. By test and trial, the process needs to be repeated for only one time and the obtained out-of-plane position as $z'_{d,i}$ is accurate enough.

Besides the modification of the processing method, parallel processing is also applied to the script to speed up the processing. Parallel processing is to distribute the repeating works (e.g. loops) in the script to multiple CPU cores to speed up the entire process. Because the machine used is a remote cluster server with workstations, message passing interface (MPI) is applied in the script. MPI allows a head core ("core#0") to distribute data to other cores and gather results from them. The memory sharing technique helps to reduce the data transfer between cores. The digital holograms can be restored in the RAM and

the only data need to be distributed are the distance or the number of windows. Other than the time of distributing and gathering data, the head core can also process a portion of the data. Based on this principle, when the number of work is indivisible by the number of cores, the workload of the head core is reduced. The reconstruction process and the whole particle detection process are both loop-intensive process so that MPI can reduce the time consumption significantly. In the reconstruction process, reconstructed images are created at 500 to 1000 distances so that the work of the reconstruction can be distributed based on the distance. Also, the minimum intensity map and the maximum Tenengrad map can be obtained as each reconstructed image is created. In the particle detection process, windows are created to enclose the particles. So the work of this part can be distributed based on the windows. However, by increasing the number of cores, the time consumption is not monotonically decreasing. For a given job, there is a certain number of cores used to reach the best time efficiency. The process of searching for the best number of cores for the HYBRID method and refinement process is included in section 5.1.2.2.

5.1.2 Test Methods

The modified HYBRID method and refinement process are tested with simulated particle holograms, which has no noises compared to the holograms recorded in experiments. Then, the test results represent the best performance of the holography methods in terms of both time consumption and accuracy. To evaluate the tests, the time consumption and accuracy test are averaged by repeating 100 times with different synthetic holograms.

5.1.2.1 Synthetic Hologram Generation

There are several methods to generate synthetic holograms, based on light diffraction theory (Zhang et al., 2006; Soulez et al., 2007; Guildenbecher et al., 2013a) and light scattering theory (Wu et al., 2012). Among them, the most accurate method is the near-field Lorenz-Mie scattering theory (Slimani et al., 1984). However, in most DIH experiments, the light diffraction theory fits the experimental conditions better. The Fresnel number $F = D_0^2/4\lambda z_0$

is used to distinguish the near-field ($F \gg 1$) and far-field ($F \leq 0.25$) diffraction, where D_0 is the particle diameter and z_0 is the distance between the particle and the hologram plane. When $F < 0.16$ the difference between the holograms simulated with the Fresnel diffraction theory and the far field version of near-field Lorenz-Mie theory are small enough to be neglected (Slimani et al., 1984). As the same quality of hologram simulated, the selection of the two methods is determined by other parameters. To test the modified HYBRID method and refinement process, thousands of synthetic holograms are generated. Thus, the method cost less time is selected, which is the Fresnel diffraction method.

The process to generate synthetic holograms is to set up particles randomly deployed at different positions and diameters. Then a plane wave is simulated to illuminated the particles. The diffracted waves propagate to the hologram plane and summed up to create the synthetic hologram. The process to generate synthetic holograms is similar to the inverse of the reconstruction process. So the reconstruction formula (Equation 2.4) can be used with replacing the hologram ($h(\xi, \eta)$) and the reference wave ($R * (\xi, \eta)$ by the mask function of a spherical particle ($p_i(x', y')$) and the complex amplitude of the light illuminated on the particle ($E_{b,i}(x', y')$), respectively. The mask function of a spherical particle is expressed as (Gao et al., 2013)

$$p_i(x', y') = \begin{cases} 0, \ \sqrt{(x_i' - x')^2 + (y_i' - y')^2} \leq r_i \\ 1, \ \sqrt{(x_i' - x')^2 + (y_i' - y')^2} > r_i \end{cases}, \tag{5.1}$$

where r_i is the radius of the ith spherical particle and (x_i', y_i') is the in-plane position of the particle. With the replacement of these two functions, Equation 2.4 can be written as

$$h_i(\xi, \eta) = |[E_{b,i}(x', y')p_i(x', y')] \otimes g(x', y', z_i)|^2, \tag{5.2}$$

where z_i is the distance between the particle and the simulated recording plane. By applying the discrete fast Fourier transform, Equation 5.2 can be rewritten as (Gao, 2014)

$$h_i(m, n) = \left| FFT^{-1} \left\{ FFT \left\{ E_{b,i}(k', l')p_i(x', y') \right\} \exp \left[jkz_i \sqrt{1 - (\tfrac{m'\lambda}{M'\Delta x'})^2 - (\tfrac{n'\lambda}{N'\Delta y'})^2} \right] \right\} \right|^2, \tag{5.3}$$

where M' and N' are the number of pixels in the $x' - y'$ direction in the synthetic hologram plane, respectively. $\Delta x'$ and $\Delta y'$ are the pixel size in the synthetic hologram and they satisfy

$\Delta x' = \Delta\xi$ and $\Delta y' = \Delta\eta$. The results from FFT and FFT^{-1} operation are 2D periodic signal in spatial frequency domain. Thus, if M' and N' are not large enough, the synthetic hologram will be the repetition of the simulated wave as shown in Fig. 5.2 (a). The actual particle field contains only one particle of $50\mu m$ at the center of the hologram plane and the distance between the particle and the hologram plane is $100mm$. Based on this problem, the synthetic hologram for the study in the paper is set to $1024 * 1024$ pixels with pixel size of $7.4 \times 7.4\mu m^2$. When the particle is close the edge of the hologram plane, the hologram of the particle will exceed the edge of the image. The exceeded part appears on the other side of the hologram as shown in Fig. 5.2 (b). To get rid of this problem, the volume for the particle field is only the center part of the hologram plane. In this study, only the center $6,000 \times 6,000\mu m^2$ is used for random particle in-plane $(x' - y')$ position. By contrast, Gao (Gao et al., 2013) created a larger synthetic hologram with double M' and N'. Then only the center $M' * N'$ pixels were cut and used as the final synthetic hologram. However, this resulted in unstable number of particles enclosed in the final synthetic hologram although the synthetic hologram has no waste pixels at the edge. Also, as the Fresnel number requirement of $F < 0.16$, the particle distance z_i for $50\mu m$ diameter particle should be larger than $7.34mm$ while the particle distances used in this study ranges from $145mm$ to $155mm$ which is much larger than the requirement.

In addition, when the cross-section of the particle is circular, an analytical expression of the synthetic hologram can be derived based on the Fresnel diffraction theory. The hologram of a spherical particle at the distance z_i from the hologram plane with radius r_i can be written as (Guildenbecher et al., 2013a)

$$h_i(\rho, Z_i) = \left| 1 - j\pi \exp\left(\frac{-j\pi\rho^2}{Z_i}\right) \left[L(u,v) - M(u,v)\right] / Z_i \right|^2, \tag{5.4}$$

where ρ is the normalized radial coordinate, $\rho = \sqrt{\xi^2 + \eta^2}/r_i$ and Z_i is the inverse of the Fresnel number, $Z_i = z_i\lambda/r_i^2$. u and v are two variables defined as $u = 2/Z_i$ and $v = 2\rho/z_i$ for $L(u,v)$ and $M(u,v)$ which are the solutions to the Lommel's integral. The integral can be expressed in the form of $L(u,v)$ and $M(u,v)$ as

$$\int_0^1 J_0(\rho v) exp\left(\frac{-ju\rho^2}{2}\right) \rho d\rho = \frac{[L(u,v) - M(u,v)]}{2}, \tag{5.5}$$

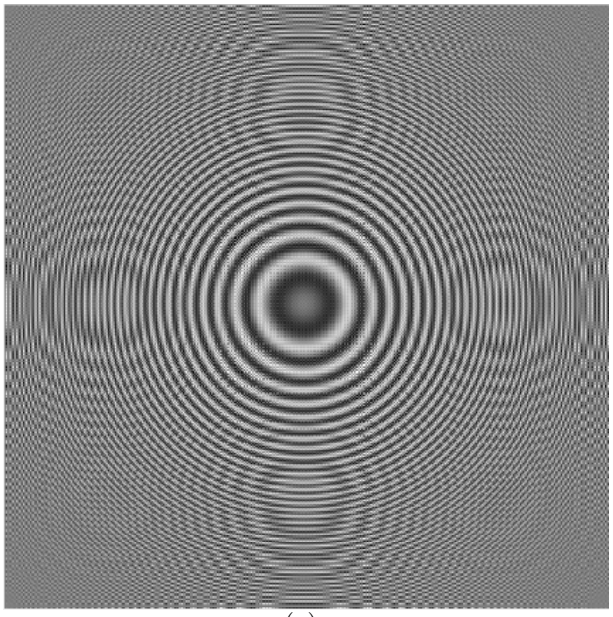

(a)

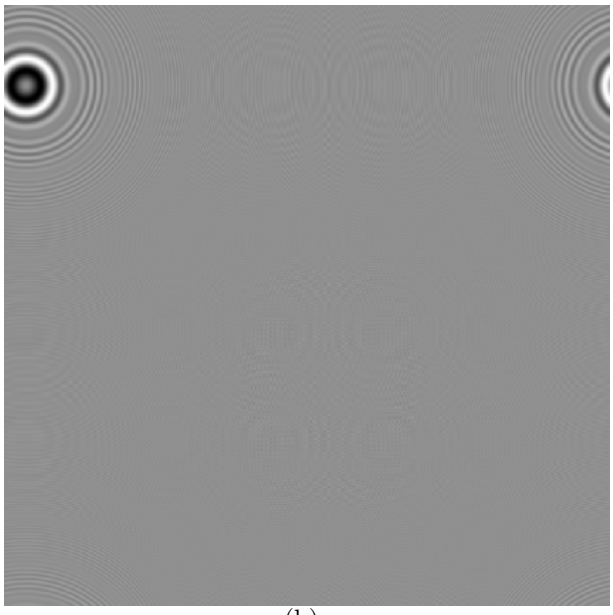

(b)

Figure 5.2. False synthetic hologram due to (a) too small number of pixels ($M' = N' = 128$) with $7.4 \times 7.4\mu m^2$ and $532nm$ wavelength and (b) the particle is close to the edge.

where J_0 is the zero-order Bessel's function. By digitizing the result from the analytical expression, the synthetic hologram can be obtained. Compared to the method of using FFT and FFT^{-1} as illustrated in Equation 5.3, the synthetic hologram generated from the analytical expression has fewer noise points. The analytical expression can be used for spherical particle simulation.

In this study, 100 different synthetic holograms are generated and 70 spherical particles are simulated in each hologram. The centers of the 70 particles are randomly distributed in a volume of $6 \times 6 \times 10mm^3$ where $10mm$ is in the z direction. The distance between the nearest surface of the particle field and the hologram plane is $145mm$. The hologram image has the size of $1,024 \times 1,024$ pixels with $7.4 \times 7.4\mu m^2$ pixel size. The diameter range of 50 holograms is $50\mu m - 200\mu m$ while that of another 50 holograms is $50\mu m - 500\mu m$. The sample synthetic holograms for each diameter range are shown in Fig. 5.3 (a) and (b), respectively. The shadow density (SD) (Lamadie et al., 2012) is calculated to evaluate how dense the particles are in the particle field. SD is defined as the ratio of the sum of the cross-section area of the particles over the cross-section area of the hologram. When the hologram satisfies $SD > 0.1$ (Malek et al., 2004), the hologram is considered as too dense so that the errors of 3D position and diameter of the particles are influenced by the light scattered from other particles. The SD of the holograms with the two kinds of diameter ranges are 0.015 and 0.072, respectively, which are both less than 0.1. The wavelength used for the synthetic hologram is set to $532nm$. The reconstruction range is set to $140mm$ to $160mm$ with separating the range to 1000 reconstruction planes equally spaced by $\Delta z = 20\mu m$.

5.1.2.2 Time Test Method

The time consumption of the modified Python script described in this work is compared to that of the existing Matlab script (Guildenbecher et al., 2014). To ensure the time measurement of the two programming language being comparable, the system CPU time is recorded and analyzed for both methods. In Matlab, *tic* and *toc* commands are used to enclose the processing code in between to measure the elapsed time of the code. In Python,

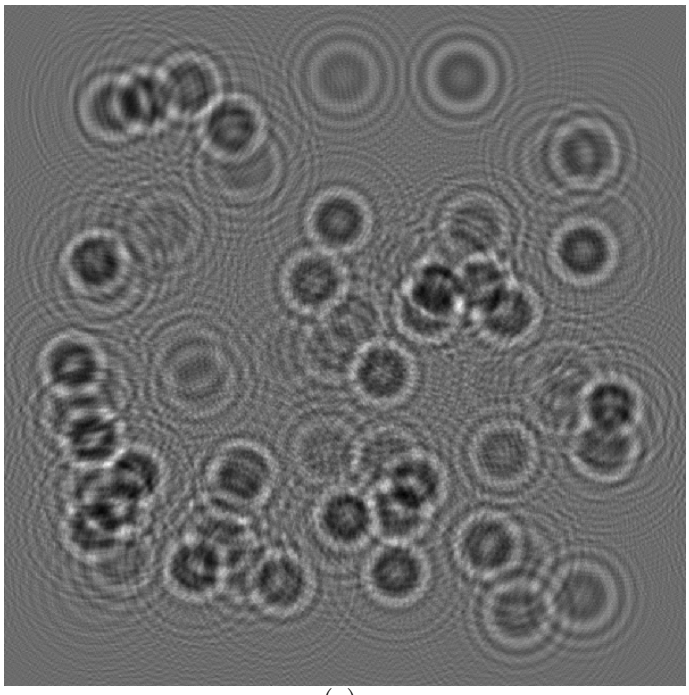

(a)

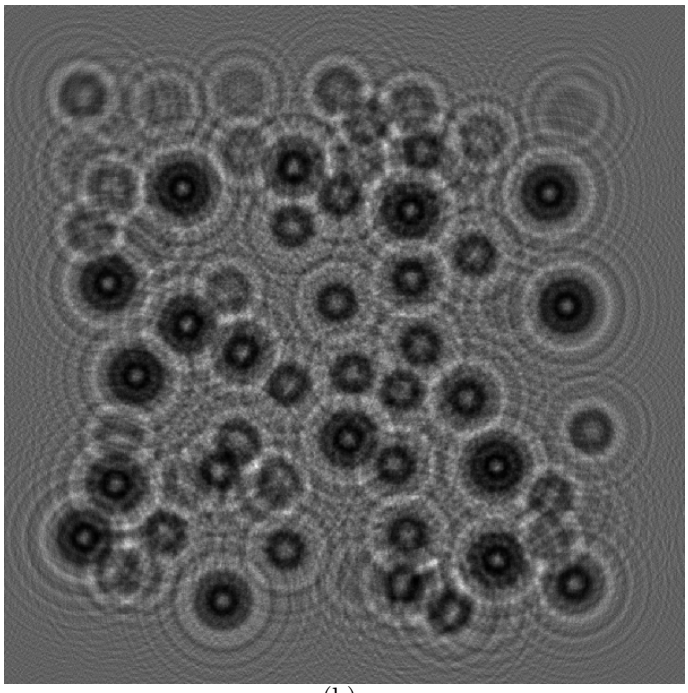

(b)

Figure 5.3. Sample synthetic with the (a) diameter range of $50\mu m - 200\mu m$ and (b) diameter range of $50\mu m - 500\mu m$.

The module *time* needs to be imported. The function *time*() can record the current system CPU time. The difference between the recorded time at the beginning of the code and at the end of the code is the elapsed time. The Matlab code from Guildenbecher (Guildenbecher et al., 2014) consists of an implement GPU speed up for the reconstruction part. However, the remote cluster of the workstation being used in this study does not have a GPU. So the Matlab code is running both on the remote cluster and on a local workstation with a comparable CPU and a GPU. The time consumption of the Matlab script on the two machines are both compared with the python script which is tested on the remote cluster to see how the CPU can reduce the processing time. The specification of the remote cluster is dual Intel Xeon Gold 5118 processor with 12 cores each at 2.3GHz base frequency. To use the remote cluster efficiently, Engineering Computing Network creates a processing queue for the cluster. The cluster can distribute computing resources to the processing codes in the queue. The user needs to use the *qsub* command to submit the processing request to the queue. The command should include the number of cores needed, the number of MPI ranks, the approximate upper limit processing time and the filename of the code. In this test, 8 cores are used to perform 8 ranks MPI on the code. The cluster will automatically terminate the processing if the result is not given after 10 hours. The local work station consists of dual Intel Xeon E5-2697v3 with 14 cores each at 2.6GHz base frequency as CPU. The GPU on the local workstation is NVIDIA Tesla K40c which is a commonly used computational GPU. Although the remote cluster has fewer cores and lower base frequency CPU, the new infrastructure of CPU can improve the performance of the machine.

For the reconstruction part, the Python code included all 4 approximation methods mentioned in section 2.3. The time consumption for the 4 reconstruction methods are measured and compared to find out the most time efficient reconstruction method. The exist Matlab script used the angular spectrum method to process reconstruction. All the time consumption test for the Matlab code is based on using this reconstruction approximation.

As discussed in section 5.1.1, the Python script uses MPI technique to apply parallel processing. However, the data transmitting process between the head core and other cores consumes time so the processing time is not always decreasing as the number of cores used

increases. By measuring and plotting the processing time of the Python script with MPI with different number of cores. The best number of cores for the HYBRID method and the refinement process can be found. It is noticed that the best number of cores is based on the number of work which is related to the number of reconstructed images and the number of particles in the hologram. For the easiness of the test, 70 particles are simulated in the synthetic hologram and to make the synthetic hologram more similar to the experiment recorded hologram. In addition, the time consumption of the reconstruction part is also recorded and compared to show how GPU and CPU differ in parallel processing.

5.1.2.3 Accuracy Test Method

With the improvement of the processing speed by modifying the HYBRID method and refinement process as described in section 5.1.1, the accuracy of the new method should be close to the existing one. Synthetic holograms are created with the method described in section 5.1.2.1.

Different parameters are calculated to characterize the accuracy of the method. The first one is the detection rate which refers to how accurate the particles in a synthetic hologram are separated. By comparing the 3D position and diameter measured by the modified HYBRID method with the true values that are used to generate the synthetic hologram, the matched particles are considered as correctly identified particles. Other particles that cannot be matched are separated into two categories. One is the particles that are not showing in the calculation results, also called missing particles. The other is the particles whose calculated diameters are significantly larger than the true value, indicating that multiple neighbor particles are identified as a single particle. In other words, the neighbor particles are not separated correctly. With this comparison, the detection rate (R_d), missing rate (R_m) and false separation rate (R_{fs}) are defined as the ratio of the number of the three categories

of particles (N_d, N_m and N_{fs}) over the total number of the particles in the particle field ($N_{tot} = 70$), respectively:

$$\begin{aligned} R_d &= \frac{N_d}{N_{tot}}, \\ R_m &= \frac{N_m}{N_{tot}}, \\ R_{fs} &= \frac{N_{fs}}{N_{tot}}. \end{aligned} \tag{5.6}$$

By averaging the three rates for the 50 different synthetic holograms of each particle diameter range, the results are compared between the existing HYBRID method with refinement and the modified method described in this paper.

Only for the correctly detected particles, the calculation of the errors of the 3D position and diameter can represent the errors of the methods. The in-plane ($x - y$) position, out-of-plane (z) position and diameter are used to evaluate error. The relative in-plane error is defined as the in-plane distance between the center of the particle of the calculated result and true value over the true particle diameter:

$$e_{planar} = \frac{\sqrt{(x - x_t)^2 + (y - y_t)^2}}{D_t}, \tag{5.7}$$

where the subscript t denotes the true value in the synthetic holograms. The correctly detected particles are paired with the corresponding synthetic particles in the simulation. The error in the out-of-plane position is defined as the relative depth error (Gao, 2014),

$$e_{depth} = \frac{|z - z_t|}{D_t}. \tag{5.8}$$

The error in diameter is defined as the relative diameter error,

$$e_D = \frac{|D - D_t|}{D_t}. \tag{5.9}$$

These three errors are also averaged by the 50 synthetic holograms of each particle diameter range. The results, the mean errors, were compared between the two methods.

5.2 Results

5.2.1 Time Test Result

For the existing Matlab script of HYBRID and refinement created by Guildenbecher (Guildenbecher et al., 2014), the time consumption with and without GPU speedup are measured as shown in Table 5.1. The GPU is only applied to the reconstruction part since, for the particle detection parts, the morphology functions does not have GPU-applicable version in Matlab. All results are the averaging results of the 50 synthetic holograms of each particle diameter range.

Table 5.1. Time consumption of different parts of the exist Matlab script with GPU option (Others included the reading image, writing output data and etc.).

	Without GPU		With GPU	
Diameter range	50 to 200μm	50 to 500μm	50 to 200μm	50 to 500μm
Reconstruction	241.323s	274.182s	1.294s	2.075s
Particle Detection	1452.611s	1509.459s	1490.120s	1562.947s
Others	14.125s	14.692s	15.423s	14.971s
Total	1707.059s	1798.333s	1506.837s	1579.993s

For the modified Python script, without MPI speed up, the time consumptions of the 4 reconstruction approximation methods are measured, respectively. The results are shown in Table 5.2. With the reconstruction method selected as angular spectrum, the time consumption for single core processing from the Python script are shown in Table 5.3.

With MPI speed up for the Python script, the plot of time consumption vs. the number of cores and the whole process for different parts with different diameter ranges are shown in Fig. 5.4 (a) to (f). The most time efficient MPI number of cores for reconstruction, particle detection and the total time were 14 cores, 6 cores and 7 cores. The two particle diameter ranges had the same result.

Table 5.2. Time consumption of the reconstruction part with different approximation methods in Python script.

Diameter Range	50 to 200μm	50 to 500μm
Angular Spectrum	282.314s	306.723s
Convolution	336.921s	369.204s
Fresnel Approximation	376.781s	409.470s
Wavelet Approximation	334.129s	370.811s

Table 5.3. Time consumption of different parts of the entire process in Python script with angular spectrum approximation methods for reconstruction.

Diameter Range	50 to 200μm	50 to 500μm
Reconstruction	282.315s	306.722s
Particle Detection	1343.810s	1409.252s
Others	11.987s	12.562s
Total	1638.112s	1728.536s

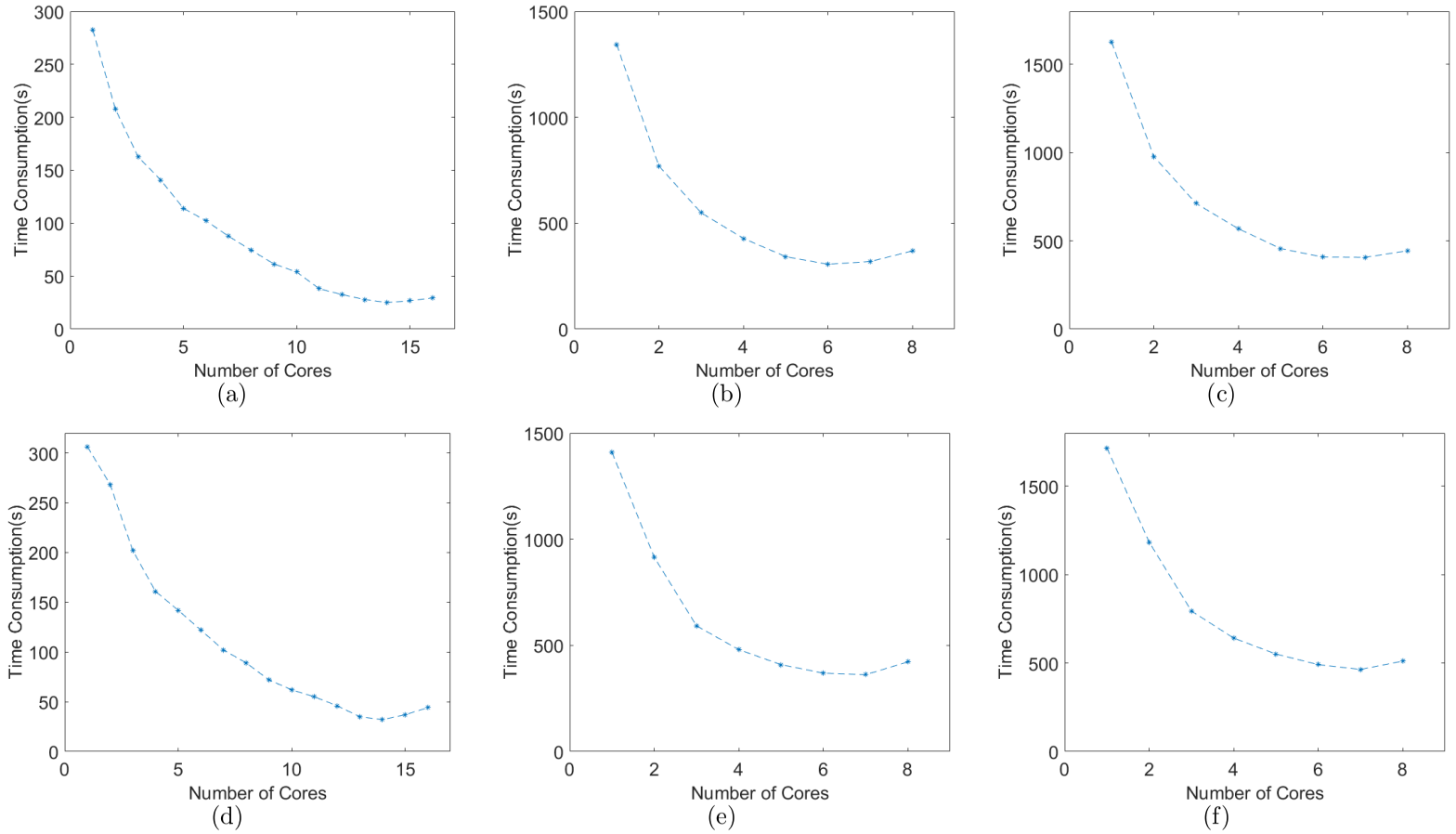

Figure 5.4. Time consumption for different parts of the Python scripts: (a) reconstruction for 50 to 200μm diameter, (b) particle detection for 50 to 200μm diameter, (c) total time for 50 to 200μm, (d) reconstruction for 50 to 500μm diameter, (e) particle detection for 50 to 500μm diameter, and (f) total time for 50 to 500μm diameter.

5.2.2 Accuracy Test Result

With running the Python script discussed in section 5.1.1, the 2 sets of synthetic holograms based on different particle diameter ranges are processed. The 3D position and particle size information are recorded as data files. The visualized results are shown in Fig. 5.5.

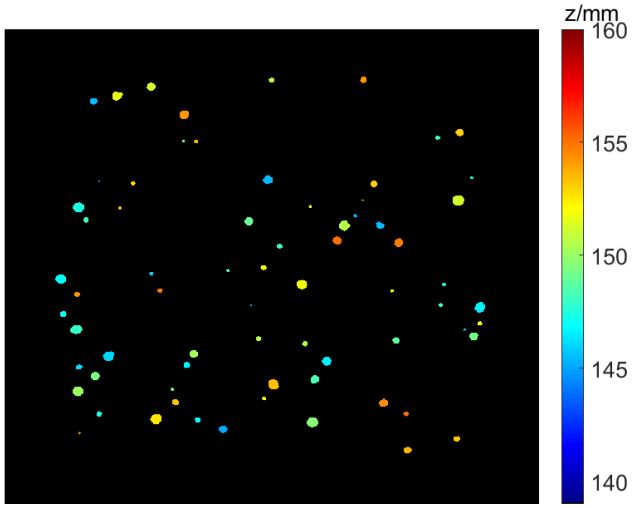

(a)

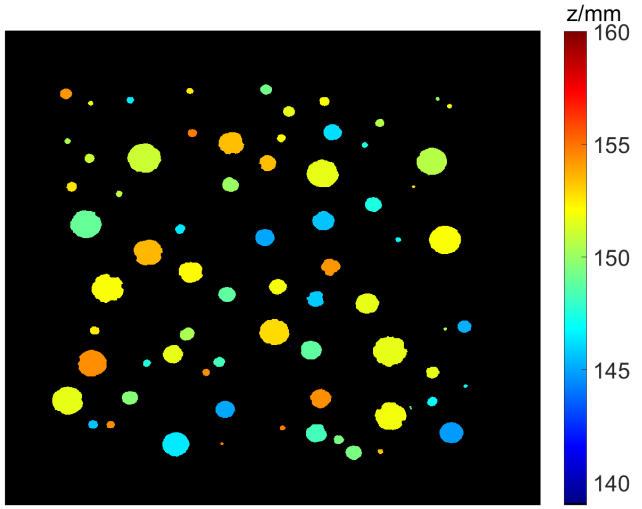

(b)

Figure 5.5. Visualized results calculated from the sample holograms in Fig. 5.3 (a) and (b), respectively.

The detection rate, missing rate and false separation rate for the two particle diameters of the exist Matlab script (HYBRID method with refinement) and Python script (modified method) are measured and averaged with the 50 synthetic holograms as shown in Table 5.4. For the correctly detected particles, the relative mean errors mentioned in section 5.1.2.3 are calculated and the results are shown in Table 5.5.

Table 5.4. The average detection rate, missing rate, and false separation rate of the existed HYBRID method and modified method for different particle diameter ranges.

	HYBRID method with refinement		Modified method	
Diameter Range	50 to 200μm	50 to 500μm	50 to 200μm	50 to 500μm
R_d	99.97%	89.11%	99.94%	86.54%
R_m	0.00%	5.17%	0.00%	5.43%
R_{fs}	0.03%	5.72%	0.05%	7.81%

Table 5.5. Mean errors of the existed HYBRID method and modified method for different particle diameter ranges.

	HYBRID method with refinement		Modified method	
Diameter Range	50 to 200μm	50 to 500μm	50 to 200μm	50 to 500μm
e_{planar}	0.46%	0.47%	0.49%	0.89%
e_{depth}	1.27%	17.42%	1.90%	19.15%
e_D	2.44%	9.03%	2.58%	13.22%

5.3 Discussion

By comparing the results of time consumption and accuracy covered in Chapter 5.2, the performance of the modified method can be analyzed. Also, future optimization of the present method can be obtained.

5.3.1 Performance of Time Reduction

In Table 5.2, the time consumption of the four reconstruction approximations are compared. The angular spectrum method spends the shortest time. The convolution method and wavelet approximation method spend similar time in reconstruction. The Fresnel approximation is abandoned for its high time consumption and the scaling problem mentioned as Equation 2.20. In this study, the angular spectrum method is applied to the Python script in comparison for the best time efficient. However, the other reconstruction methods are also incorporated in the script for selection by the user.

By comparing the time consumption in Table 5.3 and the time consumption without GPU in Table 5.1, the total processing time of the Python script is 5% less than the existing Matlab script. In addition, the performance of the machines for the two scripts are different. By comparing the reconstruction time with the angular spectrum method in Table 5.1 and Table 5.2, the machine for the Matlab script is 15% faster than the one for Python script which is consistent with the difference in the base frequency, 2.6GHz and 2.3GHz, respectively. The difference between the programming platforms (Matlab and Python) also contributes to the performance difference. Considering this machine performance difference, the modified method in Python should be around 20% faster than the exist HYBRID method with refinement in Matlab. This acceleration is the result of the modification of the thresholding process as described in section 5.1.1. In addition, increasing the size of the particles also increases the processing time because the larger particles have more edge pixels and have a higher possibility to overlap.

The performance of MPI is also analyzed. In Fig. 5.4, the reduction of the process with MPI is shown. The figures demonstrate that, at a certain number of cores for parallel

processing, the processing time reaches a minimum at a certain value called time optimization number (TON). In different parts of the method, the TON are different. TON is related to the number of jobs to be distributed. The reconstruction process has 1000 reconstructed images to be created, which are considered as 1000 jobs. The TON for the reconstruction process is 14 as shown in Fig. 5.4 (a) and (d). In contrast, the number of the windows in this study should be around 70 which is the number of the particles in the hologram, so there are around 70 jobs in the particle detection process. The TON for the particle detection part is 6 as shown in Fig.5.4 (b) and (e). It can be concluded that the TON increases as the number of jobs increase. Combining the reconstruction and particle detection process, the TON for the entire process is 7. Considering the machine used for the Python script has 24 cores in total, 6 cores are used for the Python script so that 4 holograms can be processed in parallel. Also, as shown in Fig. 5.4 (c) and (f), the difference between the time consumption with 6 cores and 7 cores is very small. With the 6 MPI, the time consumption of the modified method in Python reaches $408.26s$ for $50-200\mu m$ particle diameter range and $491.68s$ for $50-500\mu m$ particle diameter range. Compared with the existing method in Matlab without GPU speed up, the reduction of the time consumption is around four times. Even compared to the Matlab script with GPU speed up in the reconstruction part, the 6 cores MPI Python script is no less than three times as fast as the Matlab script. The results are calculated as

$$\begin{aligned} &\frac{1707.059s}{408.26s} = 4.18, \quad \frac{1798.333s}{491.68s} = 3.66 \qquad (without\ GPU), \\ &\frac{1506.837s}{408.26s} = 3.69, \quad \frac{1579.993s}{491.68s} = 3.21 \qquad (with\ GPU). \end{aligned} \tag{5.10}$$

Table 5.1 shows that the GPU can accelerate the processing significantly. The reconstruction part is sped up by hundreds of times by applying the GPU. In the future, GPU parallel processing can also be applied to the Python script to reduce the processing time in the reconstruction part. From Table 5.1, one is noted that the time consumption in the particle detection part is much larger than that in the reconstruction part. If the commands in the particle detection part in Python have a GPU version, the total processing time of the Python script can be reduced considerably.

5.3.2 Accuracy Effect

While the time consumption is significantly decreased with the modified method in Python and application of the MPI technique, it is undesirable to affect the accuracy of the detection of the particles and the calculation of the particle position and particle diameter.

In Table 5.4, the detection rate (R_d) of the methods represents how the refinement and thresholding process perform. When the size of the particles is small ($50 - 200\mu m$), almost every particle is correctly detected with both methods. The reason is the shadow density (SD) satisfying $SD \ll 0.1$. As a result, the particles in the hologram are considered as individual particles by which the light scattered is not affected by the neighbor particles. When the size of the particles increases to $50 - 500\mu m$, SD increased to close to 0.1. The detection rate for both the methods decreases significantly while the detection rate of the modified method is 2.57% lower than the exist HYBRID method. By comparing the missing rate (R_m) and the false separation rate (R_{fs}), the modified method detects more false separation particles than the exist HYBRID method. With the simplification in the thresholding process, the optimized threshold from the modified method is considered less accurate than the HYBRID method. The inaccurate threshold results in the inaccuracy of the edge pixels determination. In the refinement process, the edge sharpness profile is plotted and the valid peaks are found in the profile. With inaccurate edge pixels, the edge sharpness is definitely inaccurate. As a result, a portion of peaks which corresponding to true particles are not correctly detected and these particles are not separated. To find out the characteristics of the missing particles and false separated particles, these incorrectly detected particles for the diameter range of $50 - 500\mu m$ are divided into groups based on their sizes. As shown in Table 5.6, most of the false detected particles are the particles smaller than $75\mu m$ diameter. The reason is supposed to be that the global threshold, used to create the binary image, is determined by the global edge sharpness of the minimum intensity maps and maximum Tenengrad maps. So the edge pixels of the small particles play a limited role in determining the global threshold. If an inaccurate global threshold is calculated, the small particles are

more likely to be missed. In addition, when a large particle overlaps with a small particle, the peak corresponded to the small particle may be ignored because it is not high enough compared to the large particle. This indicates that when the diameter range of the particles is larger, both methods lead to more incorrectly detected particles. The modified method tends to have more false separated particles. However, the increased number of false separated particles is not too high. In this study, there were 70 particles in a hologram. A 2.57% increasing of the false separated particles corresponds to $70 \times 2.57\% = 1.8$ particles. Comparing to the 4 times acceleration in the processing speed, this effect on the detection rate is acceptable.

Table 5.6. Size of the incorrectly detected particles for the exist HYBRID method and modified method.

Diameter Range	**Exist HYBRID method**		**Modified method**	
	Number	Percent	Number	Percent
$50 - 75\mu m$	317	83.20%	399	84.71%
$75 - 100\mu m$	62	16.27%	71	15.07%
$> 100\mu m$	2	0.52%	1	0.21%

Other than the detection rate, the errors in calculating the 3D position and particle size are also compared between the two methods. As discussed in section 5.1.2.3, the relative errors for the in-plane position, depth and particle size are defined as the ratio of the absolute error over the particle diameter. Based on these definitions, the larger particles have larger tolerance on the absolute errors. It is reasonable to use relative errors because the larger particles have more edge pixels, which means they have larger absolute errors.

As shown in Table 5.5, similar to the detection rate, the errors are very small when the SD is low. The mean in-plane errors for both methods are less than 1%. So the results calculated with both methods are almost identical to the true value. The depth error and diameter error are under 3% of the particle diameter, which are also small enough to be negligible. When the SD increased to close to 0.1 as for diameter range of $50-500\mu m$, the in-plane error

for both methods are still very low (< 1% of the particle diameter) although the in-plane error of the modified method is double of that of the HYBRID method. So the performance of the modified method of determining the in-plane position is good enough because this information can be extracted from the 2D minimum intensity map directly. However, for the out-of-plane position and particle diameter calculation, the errors of both methods increase significantly. Compared to the existing HYBRID method, the modified method has even higher errors. The modified method leads to 19% error in depth calculation, compared to 17% of the existing HYBRID method. But in the particle diameter determination, the error of the modified method is 13% of the particle diameter, which is nearly 1.5 times as the existing HYBRID method. This 13% relative error for the particle size calculation is still acceptable, because the algorithm of determining the particle size is the equivalent diameter. The equivalent diameter is related to the area enclosed in the polygon created with the edge pixels. The simplified thresholding process leads to inaccurate edge pixels, and results in the increasing error in determining of the particle size. Another reason is that the intensity inside a particle in the minimum intensity map is not uniform. As a result, the edge pixels determined by the binary map created with the local threshold is very different from the actual image, as shown in Fig. 5.6 because the local threshold is determined by the minimum intensity map in the window. Then the thresholding process is not repeated for each reconstructed image as it does in the HYBRID method.

Concluding from the analysis above, the accuracy of the edge pixels is essential to the accuracy of determination of the out-of-plane position and particle size. The accuracy of the edge pixels mainly relies on the accuracy of the threshold. By repeating the thresholding process for each reconstructed image in the existing HYBRID method, the error is minimized by sacrificing the processing time. The modified method improves the processing speed significantly by relaxing the tolerance of errors. Definitely, the analysis in this study is based on the specific parameters used to create synthetic holograms. If the size of the hologram, the number of particles or the volume for the particle field change, the results may be different.

In the future, except for balancing the errors and the processing speed, particle detection methods based on new algorithm can be invented. It should focus on getting rid of the

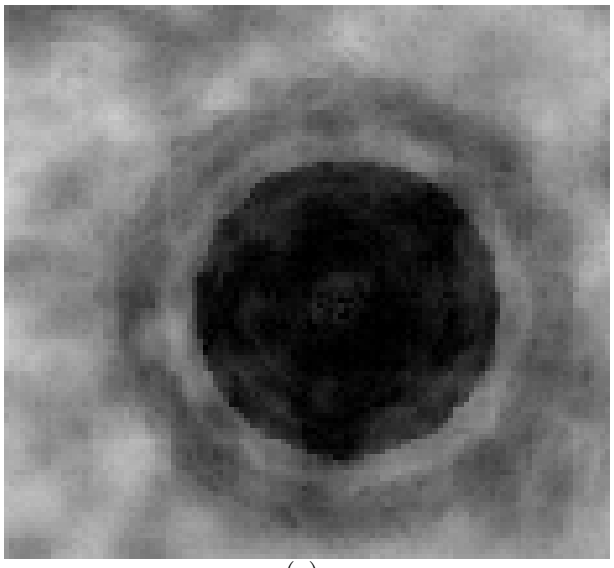

(a)

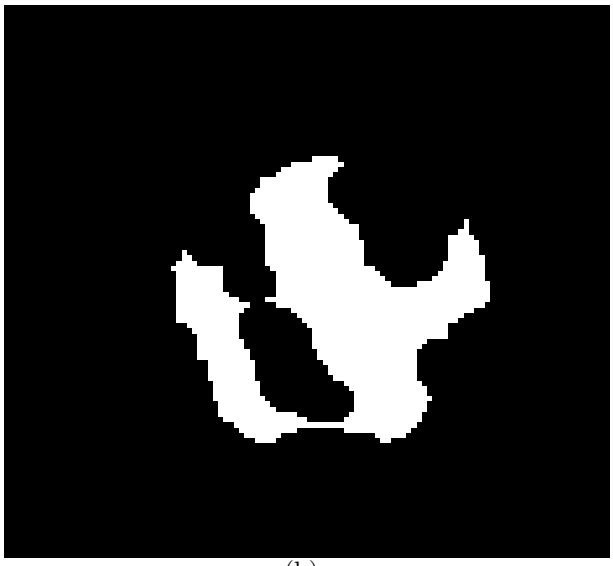

(b)

Figure 5.6. False binary map with global threshold with nonuniform intensity inside the particle in minimum intensity map. (a) nonuniform intensity inside the particle (b)False binary map created with the local threshold.

dependence on the accuracy of edge pixels. For example, algorithms based the characteristics within the window or a rim around the true edge pixels can be invented. In addition, the nonuniform intensity problem as shown in Fig. 5.6 should be resolved. Other than minimum intensity map, other maps can also be used for determining the edge pixels. GPU is another computing hardware to be used for the acceleration of the method. The comparison in section 5.3.1 shows that GPU can accelerate the processing much better than MPI. For the reconstruction part, the GPU can reduce the time consumption by more than 100 times. Although the number of jobs in the particle detection part is less than the reconstruction, GPU can still accelerate the process considerably. The only problem is the compatibility of the GPU functions in Python. For the GPU provided by NVIDIA, the CUDA platform for Python, which is the specific compiler called "Numba", has been developed. The example given by NVIDIA suggests that the CUDA platform can accelerate a computing-dense work by hundreds of times, which is suitable for image processing work. Compared to the built-in functions provided in Matlab for GPU acceleration, the "Numba" compiler needs to be installed to Python and the corresponding part of the script need to be modified to fit the requirement of the CUBA platform.

5.4 Summary

The time efficiency of the HYBRID method is optimized in ways, including picking the fastest reconstruction method, simplifying the algorithm, and applying the parallel processing method. The optimizations are fused in a self-developed Python manuscript, which is capable to perform between different platforms. Angular spectrum method spends the least time as the reconstruction method and it also gives a relatively high accuracy. In the HYBRID method, the iteration-like algorithm to find the best threshold is replaced by a fixed time optimization, which can reduce the time consumption of the particle detection process significantly with acceptable accuracy effect. MPI is selected as the parallel processing algorithm to speed up the entire manuscript with the high-performance remote workstation.

With the optimization methods applied, the new manuscript can reduce the processing time by around four times with 6 cores processing. The speed can be improved further by increasing to 7 cores. But considering the total number of cores of the workstation is 24, 6-core processing can make the workstation process 4 holograms in parallel. With the accuracy test, the new manuscript has only 2% error increase in 3D position measurements due to the reduction in iteration, which is acceptably low. The only concern is the particle size measurements. The modified method increases the particle size error by 1.5 times.

For further optimization, it is believed that GPU is capable to increase the processing speed significantly, as long as the interface for the GPU language is applied. One is noted that the work load distribution in MPI affects TON. The TON will increase if the work is distributed more carefully and effectively. Also, the Python current code has a little sacrifice on the accuracy for acceleration. A future research can be done to reach a compromise between the accuracy and processing speed. Finally, other morphology methods, e.g. dilation, etc., can help to determine the edge pixels of the particles faster and more accurate.

6. APPLICATION TO MEASURE THE DIMENSION AND MORPHOLOGY OF IRREGULAR SHAPE PARTICLES

6.1 Introduction

The dimension and morphology of solid particles are important parameters to be characterized in many industrial applications. In the coating industry, for example, the properties of coating lawyer and the performance of the coating product depend on the sizes and shapes of the coating particles (Rawle, 2002). To process wastewater with the sugar industry, the particle size affects the performance the waste removal (Gupta et al., 2003; Gupta and Ali, 2004). In the tobacco industry, manipulating the particle size of the ash is the tendency of future study and product regulation (Wayne et al., 2008). Also, The size of the particle is a key index to assess the industrial air pollution (Al-Rajhi et al., 1996).

Since DIH records out-of-focus images of the particles, the 3D information of the particles in a particle field, other than a single particle, can be extracted simultaneously from a single hologram. Several methods based on DIH have been developed to measure the size of the particles. Fraunhofer Holography (Tyler and Thompson, 1976) has been applied to quantify the particle size by analyzing the interference fringes in the holograms. Since the fringe is analyzed in one dimension, it can only measure the size of regular shape particles without rotation. Adams *et al.* (Adams et al., 1997) determine the diameter of spherical particles with uniform size. This method focuses on overcoming the high particle density by applying off-axis setup. Murata and Yasuda (Murata and Yasuda, 2000) firstly analyze the focused particles in reconstructed images. Synthetic holograms with spherical particles are analyzed with this method and the sizes of the particles are extracted accurately. One is noted that, in these methods, only synthetic spherical particles with a small particle size range are analyzed. Different than synthetic holograms, Wu *et al.* (Wu et al., 2017) apply DIH on measuring the size of particles in recorded holograms of burning particles. This study focuses on correcting

the errors caused by the flame and analyzing the number density of particles. Darakis *et al.* (Darakis et al., 2010) apply a lensed DIH to determine the sizes of ceramic, polymer and carbon fiber particles. These tiny artificial particles are in elliptical, spherical and needle shapes, respectively.

However, instead of synthetic or artificial particles, most natural solid particles, such as coating materials, have irregular shapes and usually have a wide range of sizes. As discussed in Section 3.6, the HYBRID method extracts the edge pixels of the detected particles from the reconstructed images by identifying the focused images of the particles. With these edge pixels, the dimension and morphology of the particles can be identified. For the irregular shapes, additional parameters need to be introduced to quantify the dimension and morphology of the particles. Xie *et al.* (Xie et al., 1994) apply fractal dimensions to describe the extent how the irregular shape is similar to a fine shape based on linear fitting, and its accuracy highly depends on the accuracy of linear fitting. Also, this method is less sensitive for convex polygons compared to concave polygons. Rosin (Rosin, 2004) introduces sigmoidality to describe the extent how curve the edge of the irregular shape is, by analyzing the curvature distribution of edge pixels. However, this method is very time-consuming. Stojmenovic and Zunic (Stojmenović and Žunić, 2008) introduce elongation to describe the extent how the shape is transformed from a circle. This method is noise insensitive but also insensitive when the edge of the shape is not smooth. In this study, the circularity (Žunić and Hirota, 2008; Haralick, 1974) and aspect ratio (Takashimizu and Iiyoshi, 2016) are combined to describe the irregular shape. With the advantage of DIH and adopting these parameters, a DIH-based method can be proposed to measure the dimension and morphology of irregular-shaped particles more accurately. The statistics of the parameters can characterize the dimension and morphology of a particle field. The microscopic images are taken to verify the DIH measurements.

6.2 Experimental Setup

A lensless DIH system is set up to record the unity magnification holograms for the particle field, as shown in Fig. 6.1. A continuous green laser with 500mW power and 532nm wavelength is spatially filtered and expanded to a collimated beam which fits the aperture of the camera. The collimated beam illuminates particles which suspended uniformly in distilled water in an optical cuvette. The dimension of the cuvette is $3cm$ long, $1cm$ wide and $5cm$ high. The holograms are recorded with a CCD camera (1,600 $\times$ 1,200 pixels with $7.4 \times 7.4\mu m^2$ pixel size). Three kinds of solid particles samples are analyzed in this study: Wollastonite Powder (PM), Pearl Mica Powder (PMP) and Solder Powder (SP). The concentration of the three kinds of particles are kept the same as $5mg/L$. The samples of the recorded holograms for the three kinds of particles are shown in Fig. 6.2 (a), (b) and (c), respectively.

For each kind of particle samples, 500 holograms are recorded at 18fps. To make sure the particles are not counted repeatedly, air is injected into the cuvette and the recording starts when the air bubbles are eliminated. Also, the holograms are analyzed in a five image step (e.g. Image#0, Image#5, Image#10, etc.). So 100 of the 500 holograms are analyzed with the optimized method discussed in Chapter 5.1. The edge pixels can be extracted from the focused reconstructed images of the particles. Sample reconstructed images of each kind of particle samples are shown in Fig. 6.3.

The dimension and morphology of the particles can be determined with the edge pixels extracted from the reconstructed images. To quantify the dimension and morphology of irregular-shaped particles, three parameters are introduced: equivalent diameter (D_{eq}) to quantify the size of the particles, circularity (C) and aspect ratio (γ) to quantify the morphology of the particles. D_{eq} is defined as the diameter of a circle having the same area as that of the particle (A_p) which is determined by the region enclosed by the detected edge pixels as shown in Equation 3.15 (Jennings and Parslow, 1988).

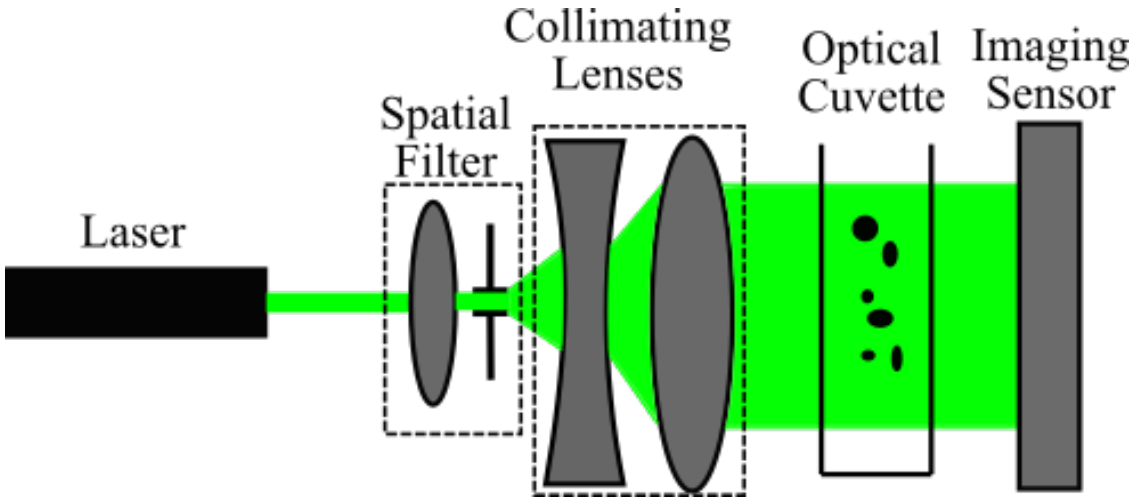

Figure 6.1. Experimental setup of the lensless DIH system.

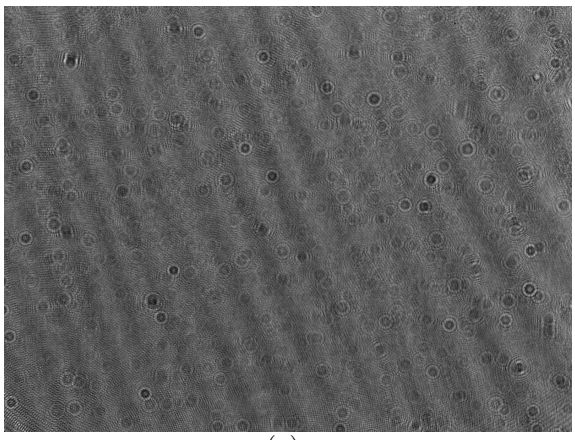

(a)

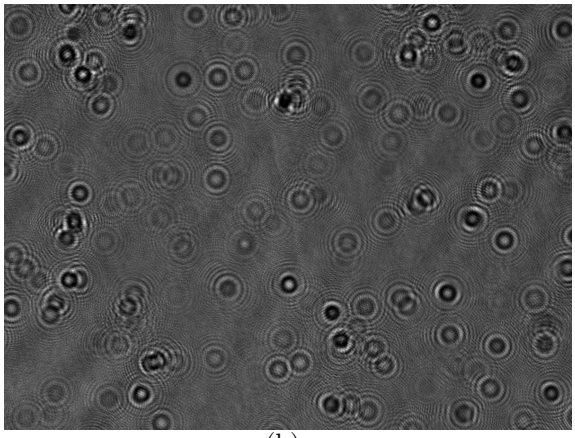

(b)

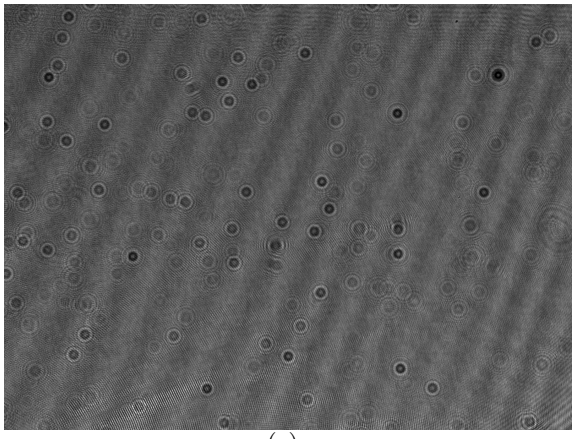

(c)

Figure 6.2. Samples of recorded holograms of (a) Wollastonite Powder, (b) Pearl Mica Powder, and (c) Solder Powder.

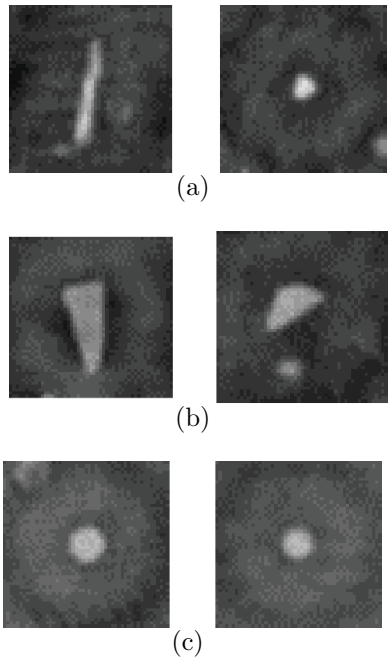

Figure 6.3. Samples images of the reconstructed particles: (a) Wollastonite Powder, (b) Pearl Mica Powder (c) Solder Powder. Images of individual particles are cropped from the reconstructed images of a group of particles.

C is adopted to describe the extent how the irregular shape is similar to a circle, which is defined as the ratio of the perimeter of a circle having the same area as the particle to the perimeter of the particle (P_p).

$$C = \frac{\pi D_{eq}}{P_p} = \frac{\sqrt{4\pi A_p}}{P_p}, \tag{6.1}$$

where P_p is determined by connecting the detected edge pixels. From the definition of the circularity, one is noted that the range of C is $(0, 1]$ and the morphology of the particle is closer to a circle as C is closer to 1. In this study, the circularity of some simple geometries are compared to the that of irregular-shaped particles to show how the particles are similar to these geometries, e.g. a equilateral triangle ($C_{tri} = 0.7776$), a square ($C_{sq} = 0.8862$) and a hexagon ($C_{hex} = 0.9523$).

Besides, γ is introduced to describe the extent how the morphology of the particle is compressed from a circular shape, e.g. into an eclipse. A rectangular with the longest length which is externally tangent to the detected edge pixels of the particle is found and γ is defined as the length ratio of the major axis to the minor axis of the rectangular.

$$\gamma = \frac{l_{max}}{l_{min}}, \tag{6.2}$$

and it is noticed that $\gamma \geq 1$.

The statistics of D_{eq}, C and γ of each kind of particle samples are analyzed to show the characteristics of the particles. The probability density function (PDF) and the cumulative density function (CDF) are plotted to show the statistics results of each kind of particle samples.

For the statistics of D_{eq}, a log-normal fit is generated to the PDF of D_{eq} for each kind of particle samples to verify the measurement. Furthermore, the Sauter mean diameter (D_{32}) of each equivalent diameter distributions are calculated to characterize the mean diameter of each kind of particle samples:

$$D_{32} = \frac{\sum_{i=1}^{N}(n_i D_i^3)}{\sum_{i=1}^{N}(n_i D_i^2)}, \tag{6.3}$$

where n_i is to the particle number in the ith bin of the D_{eq} PDF and D_i denotes the corresponding particle diameter. N denotes the number of the bins in PDF.

For the statistics of C and γ, the mean and median of each kind of particle samples are determined and compared. To compare the shape of the particles to other simple geometries, the circularity of equilateral triangle, square and hexagon (C_{tri}, C_{sq} and C_{hex}) are marked in the histogram of C for each kind of the particle samples.

Finally, microscopic images of three kinds of particle samples are taken to verify the measured results from the lensless DIH system. For Pearl Mica Powder sample and Solder Powder sample, the microscopic images are taken by an optical microscope with 100× and 200× magnification, respectively. For the Wollastonite Powder sample, since the optical microscope cannot get a focused image, a Scanning Electron Microscope (SEM) is applied with 400× magnification.

6.3 Results

For each kind of the particle samples, 100 holograms are processed. The number of the detected particles are shown in Table 6.1. One is noted that WP and PMP samples have more than 15,000 particles detected and SP sample has nearly 13,000 particles detected. The numbers of the three kinds of particles are large enough for statistical analysis. Also, since the particle solution concentration is kept the same as $5mg/L$ for all three kinds of particle samples, WP sample has the lowest average particle weight and SP sample has the largest average particle weight.

Figure 6.4 shows the statistics of the particle equivalent diameter for the three kinds of particle samples. To smooth the CDF curve, a 5-pass interpolation is applied to the raw data. The log-normal fit describes the PDF of the three kinds of particles well except for the very small particles ($< 20\mu m$). There are more small particles detected than the log-normal distribution for WP and SP samples. For the unity magnification holograms with $7.4\mu m$ pixels size, these small particles take less than 3 pixels. As a result, these small particles are not fully resolved due to the resolution limitation. One is noted that the smallest particle

detected in this study is around $15\mu m$. The smaller particles are not detected or falsely detected as larger ones. Another potential reason for this inconsistency is that the log-normal distribution does not best describe the particle diameter for these three kinds of solid particle samples. The Sauter mean diameter (D_{32}) for each kind of particle samples are calculated and listed in Tab. 6.1. The WP particles are significantly smaller than the rest two kinds of particle samples. The PMP particles are slightly larger than SP particles. The majority of the particles of WP and SP samples are small particles ($< 20\mu m$).

Table 6.1. Statistics of particle number, particle size, circularity and aspect ratio of three kinds of particles detected in 100 holograms.

Particles	Number	$D_{32}(\mu m)$	C		γ	
			Mean	Median	Mean	Median
Wollastonite Powder (WP)	15,986	36.5	0.890	0.864	1.88	1.57
Pearl Mica Powder (PMP)	15,133	58.4	0.860	0.852	1.80	1.66
Solder Powder (SP)	12,993	51.2	0.983	0.979	1.14	1.06

Figure 6.5 shows the circularity distribution of the three kinds of particle samples. The mean and median of the circularity of each kind of particle samples are included in Table 6.1. One is noted that the circularity of WP and PMP samples have a large range, which indicates that the shapes of these two kinds of particles vary significantly. The mean and median of circularity of these two kinds of particle samples are close. To be specific, a significant portion of the WP particles ($\sim 40\%$) and PMP particles ($\sim 55\%$) have a shape between square and equivalent triangle. A small portion of the WP particles ($\sim 20\%$) and PMP particles ($\sim 15\%$) has smaller circularity than equilateral triangles, which indicates that the shapes of these part of particles are very different from a circle. Another small portion ($\sim 25\%$) of the WP and PMP particles have a shape between square and hexagon, which are closer to a circle than the large portion discussed above. The shape of the other very small portion of the WP particles ($\sim 15\%$) and PMP particles ($\sim 5\%$) are very close to a circle ($C > 0.95$). In contrast, the circularity of the SP sample is close to 1 with a much

narrower range than the other two kinds of particle samples. Also, the mean and median of the circularity of the SP sample is very close to 1, which indicates that almost all of the SP particles are circular.

Figure 6.6 shows the statistics of aspect ratio of the three kinds of particle samples. The mean and median of the aspect ratio of each kind of particle samples are listed in Table 6.1. It can be found that the aspect ratio range of SP particle sample ranges from 1 to 1.5 and most of the SP particles ($\sim 70\%$) are smaller than 1.15. This means most of the SP particles are circular, which is consistent with the results analyzed from the circularity. The mean and median of the aspect ratio of the SP sample is close to 1, which supports the discussion above. WP and PMP particle samples have similar mean and median of aspect ratio, but the aspect distribution of these two kinds of particle samples are not the same. WP sample has the largest range of the aspect ratio (1 to 5), but the aspect ratio of most WP particles ($> 70\%$) are smaller than 2, which indicates that only a small portion of the WP particles display a needle-like shape. Comparing to WP particles, PMP particles have a smaller range of aspect ratio (1 to 3). The distribution of the aspect ratio of the PMP particles is more even compared to other two kinds of particles. This suggests that the PMP particles have a variety of shapes, which is consistent with the results from the circularity analysis.

To validate the dimension and morphology measurements of DIH, the microscopic images of the three kinds of particles are shown in Fig. 6.7. From the DIH measurements, WP particles have the smallest particle size while the size of the PMP particles is the largest. In the microscopic images, one is noted that most of the WP particles are tiny ($\sim 15\mu m$) and there exist a few large ones. The size of the PMP particles have a large range and are significantly larger than the WP particles, which is consistent with the DIH measurements. However, for the SP particles, the microscopic images suggest that the size of the SP particles are relatively uniform and around $50\mu m$, which is not aligned to the DIH measurements. This may result from the resolution limitation of the unity magnification holograms.

For the circularity and aspect ratio, the DIH measurements are in good agreement with the observation in the microscopic images. The DIH results suggest that the shape of all the SP particles are very close to circle, which is consistent with the particles observed in Fig.

6.7 (c). For WP particles, the DIH measurements suggest that the shapes vary significantly and very few of them are compressed heavily, which is consistent with the long needle-shape particle in Fig.6.7 (a). The microscopic image of PMP sample shows that PMP particles have a variety of shapes. This echos the wide distribution of circularity and aspect ratio measured by DIH for PMP particles. Some of the PMP particles are similar to triangles and rectangular, which meets the shape of a large portion of PMP particles are between equilateral triangle and square in DIH results.

One is noted that it is hard to describe all the morphology of the particles precisely, though the circularity of some simple geometries are compared in the analysis. It is believed that circularity and aspect ratio are only two options of parameters to describe the morphology of the solid particles. Additional parameters can be further introduced to quantify the morphology of the particles more precisely. For example, except for circularity, there can be 'rectangularity' to describe the extent how the shape is similar to a rectangular or 'trapezoidity' to show how the shapes can be categorized to different kinds of trapezoids. Also, in this study, some inconsistency occurs between the DIH measurements and microscopic observation. It is believed that the errors result from the limitation of the resolution of the unity magnification DIH system. A lens system or microscopic system can be applied to the camera to increase the magnification, which allows describing the tiny particle more accurately.

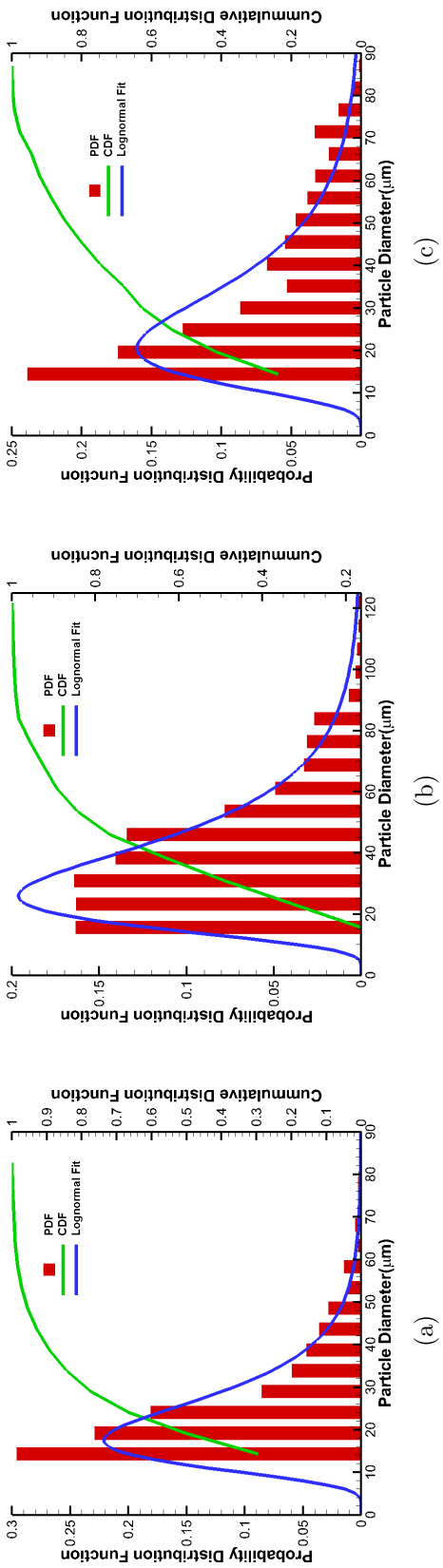

Figure 6.4. Particle diameter distribution for 3 kinds of samples: (a) Wollastonite Powder, (b) Pearl Mica Powder, and (c) Solder Powder. Log-normal fit is generated for the PDF.

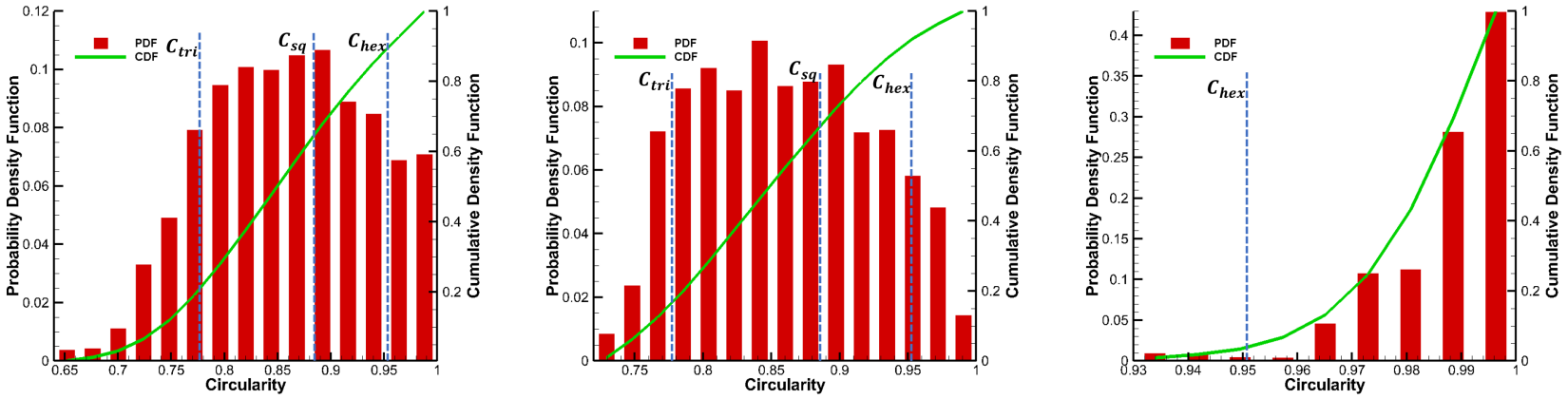

Figure 6.5. Distributions of particle circularity: (a) Wollastonite Powder, (b) Pearl Mica Powder, and (c) Solder Powder. (The vertical dash lines indicate the circularity of equilateral triangle, square and hexagon, which are C_{tri}, C_{sq}, C_{hex}, respectively.)

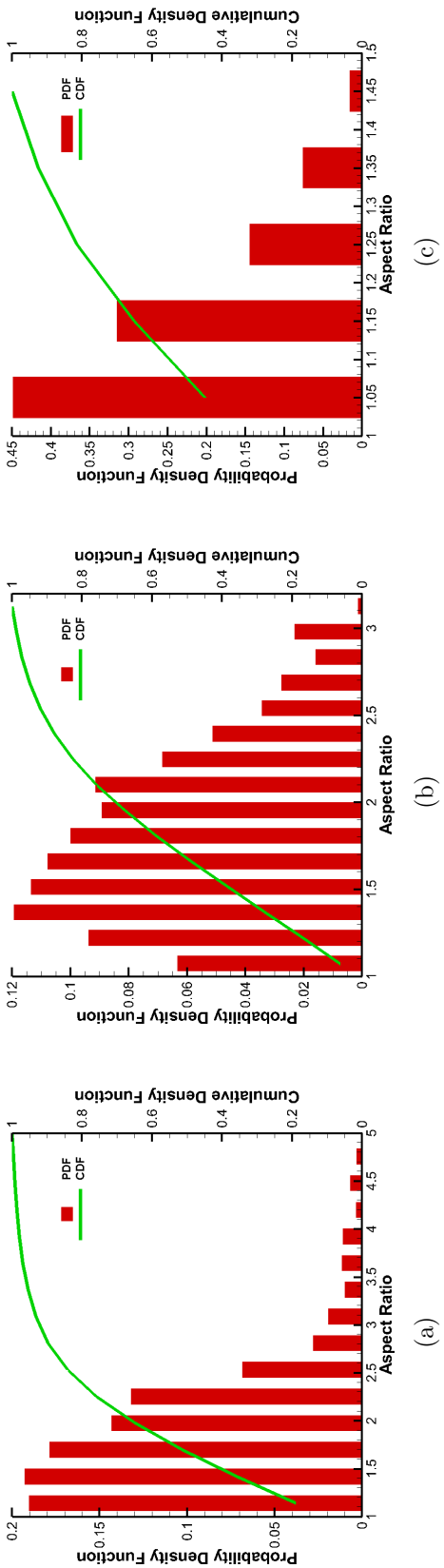

Figure 6.6. Distributions of particle aspect ratio: (a) Wollastonite Powder, (b) Pearl Mica Powder, and (c) Solder Powder.

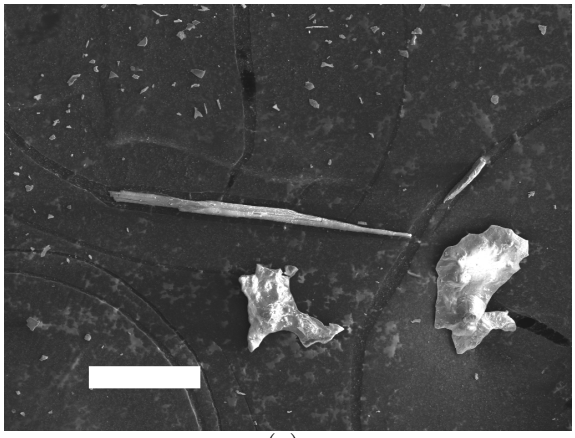

(a)

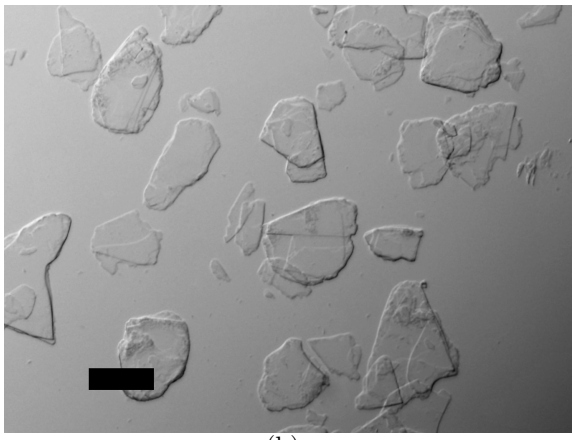

(b)

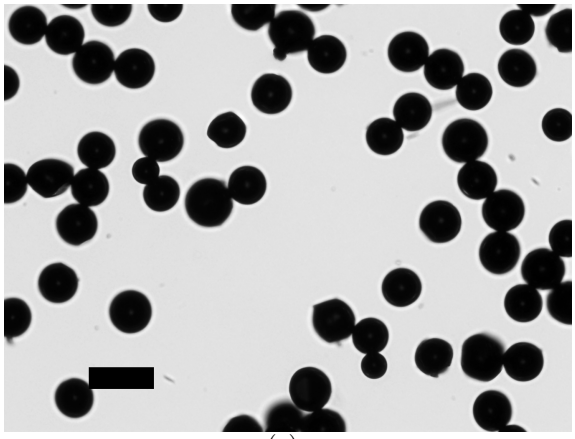

(c)

Figure 6.7. Microscopic images for the three kinds of particle samples: (a) Wollastonite Powder, (b) Pearl Mica Powder, and (c) Solder Powder. The scale bars for (a) and (c) are $50\mu m$ and the scale bar for (b) is $100\mu m$.

6.4 Summary

Unlike the droplets or synthetic particles, natural solid particles usually have irregular shapes. An experimental study is carried out to measure the dimension and morphology of irregular-shape solid particle field with DIH technique. Equivalent diameter, circularity and aspect ratio are introduced and analyzed to quantify the irregular shapes detected with DIH system. The statistics of these parameters are generated to characterize the dimension and morphology of each kind of particle samples. As DIH does not require a focused particle image, a particle field can be measured simultaneously.

Three kinds of solid particle samples are measured with a lensless DIH system. The DIH measurement results present the different dimension and morphology distribution of the three kinds of particle samples. The Wollastonite Powder sample has the smallest mean diameter while the Pearl Mica Powder particles are the largest in size. With the circularity and aspect ratio analysis, all of the Solder Powder particles are very close to circular shape while the shapes of the other two kinds of particles vary significantly. About half of the Wollastonite Powder particles and Pearl Mica Powder particles are between the shape of equilateral triangle and square. A few of Wollastonite Powder particles have large aspect ratio.

Microscopic images of the three kinds of particle samples are taken and compared to the DIH measurement results to verify that the DIH results can describe the dimension and morphology of the particle samples. The microscopic images are consistent with the DIH results except for the tiny particles ($< 20\mu m$) and the size of Solder Powder particles. As the sizes of most particles measured in this study are less than 10 times the pixel size, the resolution of the hologram affects the accuracy of the measurement to a certain extent.

There exist potentials to improve the accuracy of the present method. As discussed above, the resolution of the system is limited for the small particles. The application of a lens system or a microscope system can reduce the effective pixels size, by which more pixels can be used to describe an individual particle. The DHM technique can achieve up to $50\times$ magnification which can reduce the pixel size of the hologram to nanometer-level, which

allows the particle dimension and morphology measurements for sub-micron particles. Also, additional parameters can be introduced to describe the morphology from more aspects, which can help describe the morphology of the particles more precisely.

7. OPTIMIZATION OF LENSED DIH SETUP

As discussed in section 6.3, the accuracy of a lensless DIH system is limited by the resolution of the hologram. A lens system can be applied to DIH to improve the resolution of the holograms with large magnification. The common problem for the setup of the lensed DIH system is to optimize the position of the lens and the particle field to get the desired image resolution and magnification. In this chapter, a lens system is analyzed to determine the criteria of the setup of the lensed DIH system to achieve the desired image resolution.

A schematic of a lensed DIH system can be illustrated as Fig. 7.1. z_1 is the distance between the image plane and the particle plane. z_2 is the distance between the focal plane and the particle plane. As a lensed system is applied, there is a focal plane. We can assume that a hologram is formed on the focal plane with the lensless system. Then an image of the hologram with magnification K is formed on the image plane through the lens system. The lensed DIH system is equivalent to a lensless system with an equivalent distance z_{eq} (Wu et al., 2018):

$$z_{eq} = K^2 z_2. \tag{7.1}$$

The analysis is separated to two parts: the lens system and the equivalent lensless DIH system.

For the lens system part, a schematic of the imaging process of a lens system is illustrated as Fig.7.2. The image on the focal plane forms a real image on the image plane. s is the distance between the focal plane and lens while s' is the distance between the image plane and lens. A general lens system model is analyzed, which has a Ray transfer matrix (R_t),

$$R_t = \begin{bmatrix} A & B \\ C & D \end{bmatrix}, \tag{7.2}$$

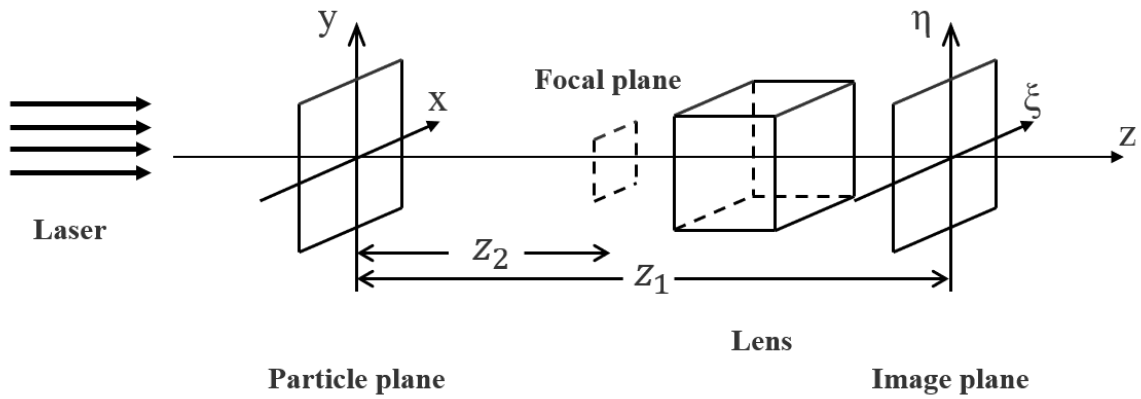

Figure 7.1. Schematic of lensed DIH system.

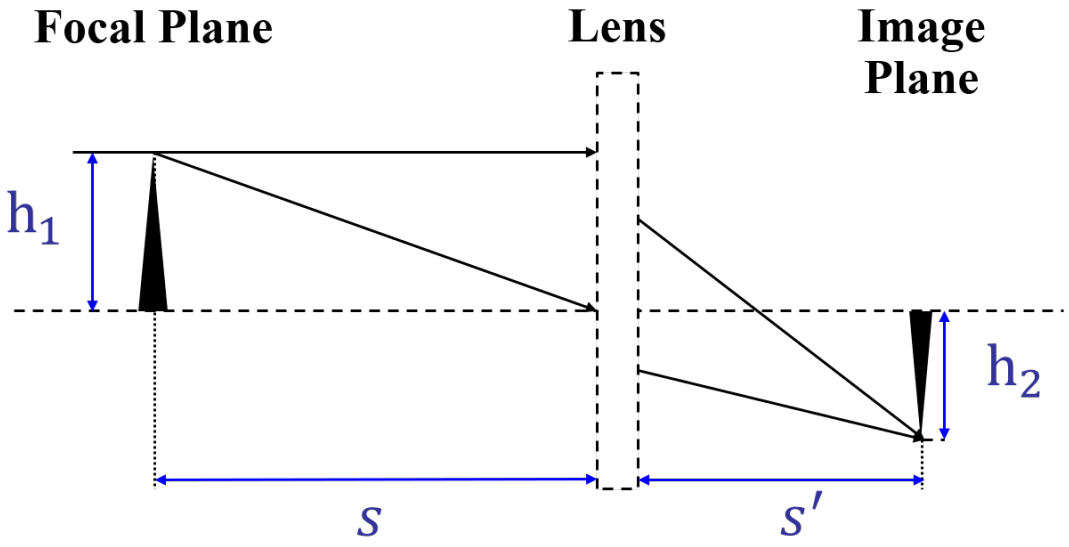

Figure 7.2. Schematic of the imaging process of a lens system.

where $C < 0$ as the horizontal light goes downward after it passes the lens. Then the two beams of the light propagate to the lens, which can be mathematically expressed as

$$\begin{bmatrix} A & B \\ C & D \end{bmatrix} \begin{bmatrix} h_1 \\ 0 \end{bmatrix} = \begin{bmatrix} Ah_1 \\ Ch_1 \end{bmatrix}, \quad \begin{bmatrix} A & B \\ C & D \end{bmatrix} \begin{bmatrix} 0 \\ -\frac{h_1}{s} \end{bmatrix} = \begin{bmatrix} -B\frac{h_1}{s} \\ -D\frac{h_1}{s} \end{bmatrix}. \tag{7.3}$$

As the two beams of light intersect after they pass the lens, two equations can be created:

$$\frac{h_2 + Ah_1}{s'} = -Ch_1, \tag{7.4}$$

$$\frac{h_2 - B\frac{h_1}{s}}{s'} = D\frac{h_1}{s}. \tag{7.5}$$

Since we want to achieve a magnification of K, we will have

$$K = \frac{h_2}{h_1}. \tag{7.6}$$

By combining Equation 7.4, 7.5 and 7.6, the distance s and s' can be expressed by the desired magnification and Ray transfer matrix:

$$\begin{aligned} s =& \frac{B - CD(K + A)}{K} \\ s' =& -C(K + A). \end{aligned} \tag{7.7}$$

Also, the distance between the focal plane and image plane is

$$\begin{aligned} z_1 - z_2 &= s + s' \\ &= \frac{B - (CD + CK)(K + A)}{K}. \end{aligned} \tag{7.8}$$

For the equivalent lensless DIH system, to simplify the analysis, the image sensor is assumed as a square sensor with $N \times N$ pixels and $\Delta\xi \times \Delta\xi$ pixel size. One is noted that if the particle field is too far from the focal plane, the resolution of the image will be decreased. But if the particle field is too close to the focal plane the fringes cannot be fully sampled. A critical distance (z_{2cr}) is developed, at which the lensed DIH system achieved the best resolution (equivalent pixel size on particle plane $\Delta x' = \frac{\Delta\xi}{K}$) without sampling problem (Wu et al., 2018):

$$z_{2cr} = \frac{N\Delta\xi^2}{K^2\lambda}. \tag{7.9}$$

If $z_2 > z_{2cr}$, the resolution of the hologram will decrease, and if $z_2 < z_{2cr}$, there will be aliasing problem. However, in DIH applications, a range of z needs to be analyzed. So the best resolution and no aliasing problem are too strict criteria. In this study, a range of z is determined based on the particle size with acceptable resolution and insignificant aliasing.

Firstly, the acceptable resolution is analyzed. To simplify the analysis, a spherical particle with diameter (d) is assumed. When the best resolution is achieved, the equivalent pixel size on particle plane is $\frac{\Delta\xi}{K}$, so the number of pixels used to describe the particle is $\left(\frac{dK}{\Delta\xi}\right)^2$. However, fewer pixels to describe the particle is also acceptable. When $z_2 > z_{2cr}$, $\Delta x'$ increase as z_2 increases (Wu et al., 2018):

$$\Delta x' = \frac{\lambda K z_2}{N\Delta\xi} \tag{7.10}$$

In our experiments, it is noticed that when a spherical particle is described by no less than 7×7 pixels, the measurements of the particle are relatively accurate. As a result, the bottom line for resolution in this study is the particle is described by no less than 7×7 pixels (Fig. 7.3):

$$\frac{d}{\Delta x'} = \frac{dN\Delta\xi}{\lambda K z_2} \geq 7. \tag{7.11}$$

The upper limit for z_2 can be determined by rearranging Equation 7.11:

$$z_2 \leq \frac{dN\Delta\xi}{7\lambda K} = \frac{dK}{7\Delta\xi} z_{2cr} \tag{7.12}$$

Then, the aliasing problem is analyzed to determine the lower limit of z_2. The reason for the aliasing problem is that the distance between neighbor fringes of the interference pattern is smaller than two times the pixel size. The schematic of the aliasing analysis is illustrated in Fig. 7.4. The particle is assumed at the center of the image (point A) and it satisfies $z_{eq} \gg \frac{N\Delta\xi}{2}$. So we can assume α is a very small angle. Point C and D are the position of two neighbor fringes at the edge of the hologram. The optical path difference between the two fringes equals to the wavelength of the light source:

$$\lambda = |AD - AC|. \tag{7.13}$$

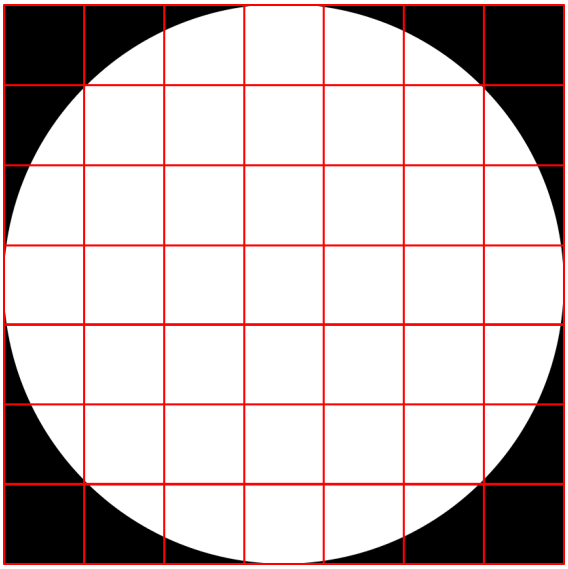

Figure 7.3. A spherical particle described by 7×7 pixels.

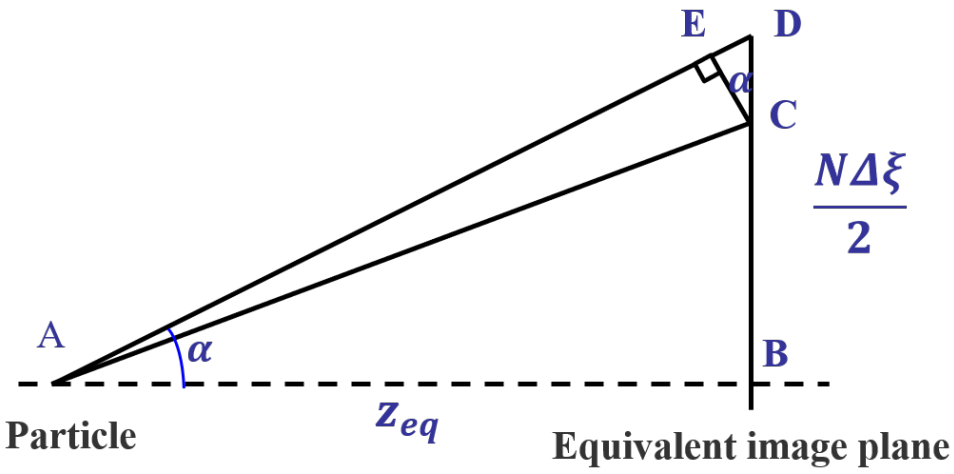

Figure 7.4. Schematic of the analysis of aliasing.

Since $\angle CAD$ is a very small angle, we can assume $AC = AE$. So it can be rewritten as $\lambda = DE$. Then the distance between the two neighbor fringes is

$$DC = \frac{DE}{\sin(\alpha)} = \frac{\lambda}{\sin(\alpha)}. \tag{7.14}$$

As α is a very small angle, $\tan(\alpha) = \sin(\alpha)$. Equation 7.14 can be written as

$$DC = \frac{\lambda}{\tan(\alpha)} = \frac{\lambda}{\frac{BD}{AB}} = \frac{2\lambda z_{eq}}{N\Delta\xi}. \tag{7.15}$$

Combined wit Equation 7.1, the distance between the two neighbor fringes can be expressed as

$$DC = \frac{2\lambda K^2 z_2}{N\Delta\xi}. \tag{7.16}$$

As discussed above, the distance between the two neighbor fringes should be larger than two times the pixel size, so we will have

$$\frac{2\lambda K^2 z_2}{N\Delta\xi} \geq 2\Delta\xi. \tag{7.17}$$

So z_2 should satisfy

$$z_2 \geq \frac{N\Delta\xi^2}{\lambda K^2} = z_{2cr}. \tag{7.18}$$

One is noted that this criterion is the most strict one because it assumes a particle at the center of the hologram and there is no aliasing on the entire hologram. However, in most holograms like Fig. 5.3 and Fig. 6.2, only a portion of the fringes are significant for reconstruction. The rest part of the interference patterns is very weak and negligible. With measurements on the synthetic holograms, it is found that the reconstruction performs well as long as the fringes 15 times larger than the particle diameter have no aliasing. As a result, the lower limit of z_2 can be determined by applying $\frac{15d}{2}$ to BD in Fig. 7.4 and Equation 7.15. At this time, DC can be expressed as

$$DC = \frac{\lambda}{\frac{BD}{AB}} = \frac{2\lambda z_{eq}}{15d} = \frac{2\lambda K^2 z_2}{15d}. \tag{7.19}$$

By applying the criterion of the distance between the two neighbor fringes should be larger than two times the pixel size, z_2 can be determined by

$$\frac{2\lambda K^2 z_2}{15d} \geq 2\Delta\xi, \qquad z_2 \geq \frac{15d\Delta\xi}{\lambda K^2} = \frac{15d}{N\Delta\xi} z_{2cr}. \tag{7.20}$$

By combining Equation 7.12 and 7.20, the accepted range of z_2 is

$$\frac{15d}{N\Delta\xi}z_{2cr} = \frac{15d\Delta\xi}{\lambda K^2} \leq z_2 \leq \frac{dN\Delta\xi}{7\lambda K} = \frac{dK}{7\Delta\xi}z_{2cr}. \tag{7.21}$$

The focal plane is a virtual plane, it is impossible to place the particle field z_2 from the focal plane. The range of z_1 can be determined by combining Equation 7.8 and 7.21:

$$\frac{15d\Delta\xi}{\lambda K^2} + \frac{B-(CD+CK)(K+A)}{K} \leq z_1 \leq \frac{dN\Delta\xi}{7\lambda K} + \frac{B-(CD+CK)(K+A)}{K}, \tag{7.22}$$

which is the range of the distance between the particle field and the image plane. Also, from Equation 7.7, the distance between the lens and the image plane should be $s' = -C(K+A)$ to achieve the magnification of K.

One is noted that the particle size d should be estimated to determine the criterion in Equation 7.22. As a result, it is recommended that a lensless DIH system can be applied first to estimate the size of the particle. Then with the estimation of z_1 and s', an optimized lensed DIH system can be set up.

8. CONCLUSION

To accelerate the processing speed of the existing HYBRID method, which is an advanced particle detection method in DIH, a modified method is developed. The modified method achieves the measurement of the in-plane $(x-y)$ position, out-of-plane (z) position and size of the particles in a volume based on the algorithm mentioned in HYBRID method (Gao et al., 2013) with refinement process (Gao et al., 2014). The acceleration methods include changing the programming environment, simplifying the redundant threshold optimization procedures and applying parallel processing technique to the script which was run on the workstation. By changing from Matlab to Python, the open source software provides more modules and functions created and optimized by the user community. Next, the threshold optimization process is reviewed and simplified. Compared to the existing HYBRID method, the modified method replaces the redundant loops with a recursion-like algorithm. In addition, the MPI technique is applied as the parallel processing technique. The TON is determined for minimizing the time consumption of the method. To characterize the degree of the acceleration methods applied, the time consumption of both the methods are tested in parts and in total. The results show that the modified method with MPI can reduce the total processing time by around 4 times. It is also believed that the application of GPU and further optimization of the algorithm can improve the processing speed more.

In contrast, it is believed that the simplification of the method will sacrifice the accuracy. The comparison of the accuracy between the HYBRID method and the modified method is made to show how this simplification affects the accuracy. Three kinds of accuracy are measured which are in-plane $(x-y)$ error, depth (z) error and diameter (D) error. The accuracy is measured in both high and low SD situation. The results show that the modified method performs not accurate enough at high SD situation in determining the out-of-plane (z) positions and particle diameters. Moreover, the particle diameters calculated by the modified method has undesirably higher errors than the HYBRID method. Therefore, the

modified method is able to shorten the processing time of digital holography which can be applied for processing numerous holograms when the requirement of accuracy is relaxed. With further modification of the methods in window searching, the accuracy of the modified method can be improved.

The application of DIH on measuring the dimension and morphology of solid particles is discussed in the last part of the thesis. A lensless DIH system is set up to record holograms for three kinds of solid particles. Equivalent diameter, circularity and aspect ratio are introduced to quantify the dimension and morphology of the particles, as well as to characterize different kinds of solid particles. Simple geometries are also compared to the morphology of the particles. Microscopic images of the particles are taken to validate the measurements of the DIH system. Because of the unity magnification, the resolution of the hologram is limited, resulting in errors in the measurements. With further applications of lens systems or microscopes, the dimension and morphology measurements can be more accurate. Also, by introducing more parameters, the morphology of the particles can be described more precisely and more details can be explored.

REFERENCES

REFERENCES

Adams, M., Kreis, T. M., and Jüptner, W. P. (1997). Particle size and position measurement with digital holography. In *Optical Inspection and Micromeasurements II*, volume 3098, pages 234–241. International Society for Optics and Photonics.

Al-Rajhi, M., Al-Shayeb, S., Seaward, M., and Edwards, H. (1996). Particle size effect for metal pollution analysis of atmospherically deposited dust. *Atmospheric Environment*, 30(1):145–153.

Ashgriz, N. (2011). *Handbook of atomization and sprays: theory and applications*. Springer Science & Business Media.

Buchmann, N., Atkinson, C., and Soria, J. (2012). Ultra-high-speed tomographic digital holographic velocimetry in supersonic particle-laden jet flows. *Measurement Science and Technology*, 24(2):024005.

Buraga-Lefebvre, C., Coëtmellec, S., Lebrun, D., and Özkul, C. (2000). Application of wavelet transform to hologram analysis: three-dimensional location of particles. *Optics and Lasers in Engineering*, 33(6):409–421.

Choi, Y.-S. and Lee, S.-J. (2009). Three-dimensional volumetric measurement of red blood cell motion using digital holographic microscopy. *Applied optics*, 48(16):2983–2990.

Darakis, E., Khanam, T., Rajendran, A., Kariwala, V., Naughton, T. J., and Asundi, A. K. (2010). Microparticle characterization using digital holography. *Chemical Engineering Science*, 65(2):1037–1044.

Denis, L., Fournier, C., Fournel, T., and Ducottet, C. (2008). Numerical suppression of the twin image in in-line holography of a volume of micro-objects. *Measurement Science and Technology*, 19(7):074004.

El Mallahi, A. and Dubois, F. (2013). Separation of overlapped particles in digital holographic microscopy. *Optics express*, 21(5):6466–6479.

Gabor, D. (1948). A new microscopic principle. *Nature*, 161:777–778.

Gao, J. (2014). *Development and applications of digital holography to particle field measurement and in vivo biological imaging*. PhD thesis, Purdue University.

Gao, J., Guildenbecher, D. R., Engvall, L., Reu, P. L., and Chen, J. (2014). Refinement of particle detection by the hybrid method in digital in-line holography. *Applied optics*, 53(27):G130–G138.

Gao, J., Guildenbecher, D. R., Reu, P. L., and Chen, J. (2013). Uncertainty characterization of particle depth measurement using digital in-line holography and the hybrid method. *Optics express*, 21(22):26432–26449.

Goodman, J. W. (2005). *Introduction to Fourier optics*. Roberts and Company Publishers.

Guildenbecher, D. R., Engvall, L., Gao, J., Grasser, T. W., Reu, P. L., and Chen, J. (2014). Digital in-line holography to quantify secondary droplets from the impact of a single drop on a thin film. *Experiments in fluids*, 55(3):1670.

Guildenbecher, D. R., Gao, J., Reu, P. L., and Chen, J. (2013a). Digital holography simulations and experiments to quantify the accuracy of 3d particle location and 2d sizing using a proposed hybrid method. *Applied optics*, 52(16):3790–3801.

Guildenbecher, D. R., Reu, P. L., Stuaffacher, H. L., and Grasser, T. (2013b). Accurate measurement of out-of-plane particle displacement from the cross correlation of sequential digital in-line holograms. *Optics letters*, 38(20):4015–4018.

Gupta, V. K. and Ali, I. (2004). Removal of lead and chromium from wastewater using bagasse fly asha sugar industry waste. *Journal of colloid and interface science*, 271(2):321–328.

Gupta, V. K., Jain, C., Ali, I., Sharma, M., and Saini, V. (2003). Removal of cadmium and nickel from wastewater using bagasse fly asha sugar industry waste. *Water research*, 37(16):4038–4044.

Haralick, R. M. (1974). A measure for circularity of digital figures. *IEEE Transactions on Systems, Man, and Cybernetics*, 4:394–396.

Jennings, B. and Parslow, K. (1988). Particle size measurement: the equivalent spherical diameter. *Proc. R. Soc. Lond. A*, 419(1856):137–149.

Katz, J. and Sheng, J. (2010). Applications of holography in fluid mechanics and particle dynamics. *Annual Review of Fluid Mechanics*, 42:531–555.

Khanam, T., Rahman, M. N., Rajendran, A., Kariwala, V., and Asundi, A. K. (2011). Accurate size measurement of needle-shaped particles using digital holography. *Chemical engineering science*, 66(12):2699–2706.

Lamadie, F., Bruel, L., and Himbert, M. (2012). Digital holographic measurement of liquid–liquid two-phase flows. *Optics and Lasers in Engineering*, 50(12):1716–1725.

Lebrun, D., Belaïd, S., and Özkul, C. (1999). Hologram reconstruction by use of optical wavelet transform. *Applied optics*, 38(17):3730–3734.

Lee, J., Sallam, K. A., Lin, K.-C., and Carter, C. D. (2009). Spray structure in near-injector region of aerated jet in subsonic crossflow. *Journal of Propulsion and Power*, 25(2):258–266.

Lee, S. J., Seo, K. W., Choi, Y. S., and Sohn, M. H. (2011). Three-dimensional motion measurements of free-swimming microorganisms using digital holographic microscopy. *Measurement Science and Technology*, 22(6):064004.

Leighton, T. (2012). *The acoustic bubble*. Academic press.

Lü, Q., Chen, Y., Yuan, R., Ge, B., Gao, Y., and Zhang, Y. (2009). Trajectory and velocity measurement of a particle in spray by digital holography. *Applied optics*, 48(36):7000–7007.

Malek, M., Allano, D., Coëtmellec, S., and Lebrun, D. (2004). Digital in-line holography: influence of the shadow density on particle field extraction. *Optics Express*, 12(10):2270–2279.

Meng, H., Anderson, W., Hussain, F., and Liu, D. D. (1993). Intrinsic speckle noise in in-line particle holography. *JOSA A*, 10(9):2046–2058.

Murata, S. and Yasuda, N. (2000). Potential of digital holography in particle measurement. *Optics & Laser Technology*, 32(7-8):567–574.

Palero, V., Arroyo, M. P., and Soria, J. (2007). Digital holography for micro-droplet diagnostics. *Experiments in Fluids*, 43(2-3):185–195.

Raffel, M., Willert, C. E., Scarano, F., Kähler, C. J., Wereley, S. T., and Kompenhans, J. (2018). *Particle image velocimetry: a practical guide*. Springer.

Rawle, A. (2002). The importance of particle sizing to the coatings industry part 1: Particle size measurement. *Advances in colour science and technology*, 5(1):1–12.

Rosin, P. L. (2004). Measuring sigmoidality. *Pattern Recognition*, 37(8):1735–1744.

Schnars, U. and Jueptner, W. (2005). *Digital Holography. Digital hologram recording, reconstruction principle, and related techniques*. Springer.

Schnars, U. and Jüptner, W. (1994). Direct recording of holograms by a ccd target and numerical reconstruction. *Applied optics*, 33(2):179–181.

Sheng, J., Malkiel, E., and Katz, J. (2008). Using digital holographic microscopy for simultaneous measurements of 3d near wall velocity and wall shear stress in a turbulent boundary layer. *Experiments in fluids*, 45(6):1023–1035.

Sheng, J., Malkiel, E., Katz, J., Adolf, J., Belas, R., and Place, A. R. (2007). Digital holographic microscopy reveals prey-induced changes in swimming behavior of predatory dinoflagellates. *Proceedings of the National Academy of Sciences*, 104(44):17512–17517.

Slimani, F., Gréhan, G., Gouesbet, G., and Allano, D. (1984). Near-field lorenz-mie theory and its application to microholography. *Applied optics*, 23(22):4140–4148.

Soulez, F., Denis, L., Fournier, C., Thiébaut, É., and Goepfert, C. (2007). Inverse-problem approach for particle digital holography: accurate location based on local optimization. *JOSA A*, 24(4):1164–1171.

Stojmenović, M. and Žunić, J. (2008). Measuring elongation from shape boundary. *Journal of Mathematical Imaging and Vision*, 30(1):73–85.

Takashimizu, Y. and Iiyoshi, M. (2016). New parameter of roundness r: circularity corrected by aspect ratio. *Progress in Earth and Planetary Science*, 3(1):2.

Tao, B., Katz, J., and Meneveau, C. (2000). Geometry and scale relationships in high reynolds number turbulence determined from three-dimensional holographic velocimetry. *Physics of Fluids*, 12(5):941–944.

Tenenbaum, J. M. (1970). Accommodation in computer vision. Technical report, Stanford Univ Ca Dept of Computer Science.

Tian, L., Loomis, N., Domínguez-Caballero, J. A., and Barbastathis, G. (2010). Quantitative measurement of size and three-dimensional position of fast-moving bubbles in air-water mixture flows using digital holography. *Applied optics*, 49(9):1549–1554.

Tyler, G. A. and Thompson, B. J. (1976). Fraunhofer holography applied to particle size analysis a reassessment. *Optica Acta: International Journal of Optics*, 23(9):685–700.

Wang, L., Feng, J., Gao, X., and Peng, X. (2017). Investigation on the oil–gas separation efficiency considering oil droplets breakup and collision in a swirling flow. *Chemical Engineering Research and Design*, 117:394–400.

Wayne, G. F., Connolly, G. N., Henningfield, J. E., and Farone, W. A. (2008). Tobacco industry research and efforts to manipulate smoke particle size: implications for product regulation. *Nicotine & Tobacco Research*, 10(4):613–625.

Wu, X., Meunier-Guttin-Cluzel, S., Wu, Y., Saengkaew, S., Lebrun, D., Brunel, M., Chen, L., Coetmellec, S., Cen, K., and Grehan, G. (2012). Holography and micro-holography of particle fields: a numerical standard. *Optics communications*, 285(13-14):3013–3020.

Wu, X., Yao, L., Wu, Y., Lin, X., Chen, L., Chen, J., Gao, X., and Cen, K. (2018). In-situ characterization of coal particle combustion via long working distance digital in-line holography. *Energy & fuels*, 32(8):8277–8286.

Wu, Y., Wu, X., Yao, L., Xue, Z., Wu, C., Zhou, H., and Cen, K. (2017). Simultaneous particle size and 3d position measurements of pulverized coal flame with digital inline holography. *Fuel*, 195:12–22.

Xie, Y., Hopke, P. K., Casuccio, G., and Henderson, B. (1994). Use of multiple fractal dimensions to quantify airborne particle shape. *Aerosol science and technology*, 20(2):161–168.

Yang, F., Manjare, M., Zhao, Y., and Qiao, R. (2017). On the peculiar bubble formation, growth, and collapse behaviors in catalytic micro-motor systems. *Microfluidics and Nanofluidics*, 21(1):6.

Yang, Y. and Kang, B. (2011). Digital particle holographic system for measurements of spray field characteristics. *Optics and Lasers in Engineering*, 49(11):1254–1263.

Yang, Y., Kang, B., and Choo, Y. (2008). Application of the correlation coefficient method for determination of the focal plane to digital particle holography. *Applied optics*, 47(6):817–824.

Zhang, F., Yamaguchi, I., and Yaroslavsky, L. (2004). Algorithm for reconstruction of digital holograms with adjustable magnification. *Optics letters*, 29(14):1668–1670.

Zhang, Y., Shen, G., Schröder, A., and Kompenhans, J. (2006). Influence of some recording parameters on digital holographic particle image velocimetry. *Optical Engineering*, 45(7):075801.

Žunić, J. and Hirota, K. (2008). Measuring shape circularity. In *Iberoamerican Congress on Pattern Recognition*, pages 94–101. Springer.

VITA

VITA

Yijie Wang was born on November 20th, 1992 in Beijing, China. In 2011, he attend Beijing Institute of Technology (BIT), Beijing, China as an undergraduate student in aeronautics and astronautics engineering and transfer to Illinois Institute of Technology (IIT), Chicago, Illinois, U.S. to continue his undergraduate study in 2013. He graduate in 2016 with Bachelor's degree from both schools. After that, he accepted the offer from the School of Mechanical Engineering at Purdue University and enrolled in the MS program. His master research focused on the optimization and application of digital in-line holography. Upon graduation in August 2019, Yijie will continue his study in a PhD program in the School of Mechanical Engineering at Purdue University.